Sizing up protoplanetary disks

Trapman, L.

4 | Observed sizes of planet-forming disks trace viscous spreading

L. Trapman, G. Rosotti, A. D. Bosman, M. R. Hogerheijde and E. F. van Dishoeck, 2020, A&A, 640, 4

Abstract

Context: The evolution of protoplanetary disks is dominated by the conservation of angular momentum, where the accretion of material onto the central star is fed by the viscous expansion of the outer disk or by disk winds extracting angular momentum without changing the disk size. Studying the time evolution of disk sizes therefore allows us to distinguish between viscous stresses or disk winds as the main mechanism of disk evolution. Observationally, estimates of the size of the gaseous disk are based on the extent of CO submillimeter rotational emission, which is also affected by the changing physical and chemical conditions in the disk during the evolution.

Aims: We study how the gas outer radius measured from the extent of the CO emission changes with time in a viscously expanding disk. We also investigate to what degree this observable gas outer radius is a suitable tracer of viscous spreading and whether current observations are consistent with viscous evolution.

Methods: For a set of observationally informed initial conditions we calculated the viscously evolved density structure at several disk ages and used the thermochemical code `DALI` to compute synthetic emission maps, from which we measured gas outer radii in a similar fashion as observations.

Results: The gas outer radii ($R_{\mathrm{CO,\ 90\%}}$) measured from our models match the expectations of a viscously spreading disk: $R_{\mathrm{CO,\ 90\%}}$ increases with time and, for a given time, $R_{\mathrm{CO,\ 90\%}}$ is larger for a disk with a higher viscosity α_{visc}. However, in the extreme case in which the disk mass is low ($M_{\mathrm{disk}} \leq 10^{-4}$ $\mathrm{M}_{\odot}$) and α_{visc} is high ($\geq 10^{-2}$), $R_{\mathrm{CO,\ 90\%}}$ instead decreases with time as a result of CO photodissociation in the outer disk. For most disk ages, $R_{\mathrm{CO,\ 90\%}}$ is up to$\sim 12\times$ larger than the characteristic size R_{c} of the disk, and $R_{\mathrm{CO,\ 90\%}}/R_{\mathrm{c}}$ is largest for the most massive disk. As a result of this difference, a simple conversion of $R_{\mathrm{CO,\ 90\%}}$ to α_{visc} overestimates the true α_{visc} of the disk by up to an order of magnitude. Based on our models, we find that most observed gas outer radii in Lupus can be explained using viscously evolving disks that start out small ($R_{\mathrm{c}}(t = 0) \simeq 10$ AU) and have a low viscosity ($\alpha_{\mathrm{visc}} = 10^{-4} - 10^{-3}$).

Conclusions: Current observations are consistent with viscous evolution, but expanding the sample of observed gas disk sizes to star-forming regions, both younger and older, would better constrain the importance of viscous spreading during disk evolution.

4.1 Introduction

Planetary systems form and grow in protoplanetary disks. These disks provide the raw materials of gas and dust to form the increasingly diverse population of exoplanets and planetary systems that has been observed (see, e.g. Benz et al. 2014; Morton et al. 2016; Mordasini 2018). The formation of planets and the evolution of protoplanetary disks are closely related. While planets are forming, the disk is evolving around them, affecting the availability of material and providing constantly changing physical conditions around the planets. In a protoplanetary accretion disk, material is transported through the disk and accreted onto the star. We are still debating exactly which physical process dominates the angular momentum transport and drives the accretion flow, which is a crucial part of disk evolution.

It is commonly assumed that disks evolve under the influence of an effective viscosity, where viscous stresses and turbulence transport angular moment to the outer disk (see, e.g. Lynden-Bell & Pringle 1974; Shakura & Sunyaev 1973). As a consequence of the outward angular momentum transport, the bulk of the mass moves inward and is accreted onto the star. The physical processes that constitute this effective viscosity are still a matter of debate, magnetorotional instability being the most accepted mechanism (see, e.g. Balbus & Hawley 1991, 1998).

An alternative hypothesis is that angular momentum can be removed by disk winds rather than being transported through the disk (see, e.g. Turner et al. 2014 for a review). The presence of a vertical magnetic field in the disk can lead to the development of a magnetohydrodynamic (MHD) disk wind. These disk winds remove material from the surface of the disk and are thus able to provide some or all of the angular momentum removal required to fuel stellar accretion (see, e.g. Ferreira et al. 2006; Béthune et al. 2017; Zhu & Stone 2018). Direct observational evidence of such disk winds focuses on the inner part of the disk, but it is unclear whether winds dominate the transport of angular momentum and therefore how much winds affect the evolution of the disk (see, e.g. Pontoppidan et al. 2011; Bjerkeli et al. 2016; Tabone et al. 2017; de Valon et al. 2020).

Observationally these two scenarios make distinctly different predictions on how the sizes of protoplanetary disks evolve over time. In the viscous disk theory, conservation of angular momentum ensures that some parts of the disk move outward. As a result, disk sizes should grow with time. If instead disk sizes do not grow with time, disk winds are likely to drive disk evolution. To distinguish between viscous evolution and disk winds we need to define a disk size, which has to be measured or inferred from observed emission, and we must examine how it changes as a function of disk age.

With the advent of the Atacama Large Millimeter/sub-Millimeter Array (ALMA) it has become possible to perform large surveys of protoplanetary disks at high angular resolution. This has resulted in a large number of disks for which the extent of the millimeter continuum emission, the dust disk size, can be measured (see, e.g. Barenfeld et al. 2017; Cox et al. 2017; Tazzari et al. 2017; Ansdell et al. 2018; Cieza et al. 2018; Long et al. 2019). However, this continuum emission is predominantly produced by millimeter-sized dust grains, which also undergo radial drift as a result of the drag force from the gas, an inward motion that complicates the picture. Moreover, radial drift and radially dependent grain growth lead to a dependence between the extent of the continuum emission and the wavelength of the observations; emission at longer wavelengths is more compact (see e.g. Tripathi et al. 2018).

Rosotti et al. (2019b) used a modeling framework to study the combined effect of radial drift and viscous spreading on the observed dust disk sizes. They determined that to measure viscous spreading, the dust disk size has to be defined as a high fraction ($\geq$ 95%) of the total continuum flux. To ensure that this dust disk size is well characterized, the dust continuum has to be resolved a signal-to-noise ratio (S/N). These authors show that existing surveys lack the sensitivity to detect viscous spreading.

To avoid having to disentangle the effects of radial drift from viscous spreading, we can instead measure a gas disk size from rotational line emission of molecules such as CO and CN, which are commonly observed in protoplanetary disks. An often used definition for the gas disk size is the radius that encloses 90% of the total CO $J = 2 - 1$ flux ($R_{\mathrm{CO,\ 90\%}}$; see, e.g. Ansdell et al. 2018). This radius encloses most ($> 98\%$) of the disk mass and it has been shown that $R_{\mathrm{CO,\ 90\%}}$ is not affected by dust evolution (Trapman et al. 2019). The longer integration time required to detect this emission in the outer disk means that significant samples of measured gas disk sizes are only now becoming available (see, e.g. Barenfeld et al. 2017; Ansdell et al. 2018). Using a sample of measured gas disk sizes collated from literature, Najita & Bergin (2018) show tentative evidence that older Class II sources have larger gas disk sizes that the younger Class I sources; this is consistent with expectations for viscous spreading. It should be noted however that the gas disk sizes in their sample were measured using a variety of different tracers and observational definitions of the gas disk size.

When searching for viscous spreading using measured gas disk sizes it is important to keep in mind that these gas disk sizes are an observed quantity that are measured from molecular line emission. As the disk evolves, densities and temperatures change, affecting the column densities and excitation levels of the gas tracers used to measure the disk size. How well the observed gas outer radius traces viscous expansion has not been investigated in much detail.

Time-dependent chemistry also affects the gas tracers such as CO that we use to measure gas disk sizes. At lower densities CO, found in the outer disk and at a few scale heights above the midplane of the disk, is destroyed through photodissociation by UV radiation. Trapman et al. (2019) show that $R_{\mathrm{CO,\ 90\%}}$ traces the point in the outer disk where CO becomes photodissociated. Deeper in the disk, around the midplane where the temperature is low, CO freezes out onto dust grains. Once frozen out, CO can be converted into other molecules such as CO_2, CH_4 and CH_3OH (see, e.g. Bosman et al. 2018; Schwarz et al. 2018). These molecules have higher binding energies than CO and therefore stay frozen out at temperatures at which CO would normally desorb back into the gas phase. Through this process gas-phase CO can be more than an order of magnitude lower than the abundance of 10^{-4} with respect to molecular hydrogen, which is the expected abundance at which most of the volatile carbon is contained in CO (see, e.g. Lacy et al. 1994).

In this work, we set up disk models with observationally informed initial conditions, let the surface density evolve viscously, and use the thermochemical code `DALI` (Bruderer et al. 2012; Bruderer 2013) to study how the CO $J = 2 - 1$ intensity profiles, and the gas disk sizes derived from these profiles, change over time. We then compare these values with existing observations to see if the observations are consistent with viscous evolution. This work is structured as follows: We introduce the setup and assumptions in our modeling in Section 4.2. In Section 4.3 we show how well observed gas outer radii trace viscous evolution both qualitatively and quantitatively.

In Section 4.4 we compare our models to observations. We also study how chemical CO depletion through grain-surface chemistry affects our results. We discuss whether external photo-evaporation could explain the small observed gas disk sizes, compare our results to disk evolution driven by magnetic disks winds, and we discuss whether including episodic accretion would affect our results. We conclude in Section 4.5 that measured gas outer radii can be used to trace viscous spreading in disks.

4.2 Model setup

The gas disk size is commonly obtained from CO rotational line observations, for example, by measuring the radius that encloses 90% of the CO flux (e.g. Ansdell et al. 2018) or by fitting a power law to the observed visibilities (e.g. Barenfeld et al. 2017). In this work we used the radius that encloses 90% of the ^{12}CO 2-1 flux ($R_{\rm CO,\ 90\%}$) as the definition of the observed gas disk size. Trapman et al. (2019) show that $R_{\rm CO,\ 90\%}$ traces a fixed surface density in the outer disk, where CO becomes photodissociated. To see if $R_{\rm CO,\ 90\%}$ is a suitable tracer of viscous evolution, we are therefore interested in how the extent of the ^{12}CO intensity changes over time in a viscously evolving disk.

Our approach for setting up our models is the following. First, we obtained a set of initial conditions that reproduce current observed stellar accretion rates, assuming that the disks feeding the stellar accretion have evolved viscously. Next we calculated the time evolution of the surface density. For each set of initial conditions, we analytically calculated the surface density profile ($\Sigma(R,t)$) at ten different disk ages. For each of these time steps we used the thermochemical code Dust and Lines (`DALI`; Bruderer et al. 2012; Bruderer 2013) to calculate the current temperature and chemical structure of the disk at that age and created synthetic emission maps of ^{12}CO, from which we measured $R_{\rm CO,\ 90\%}$.

4.2.1 Viscous evolution of the surface density

Accretion disks in which the disk structure is shaped by viscosity are often described using a $\alpha-$disk formalism (Shakura & Sunyaev 1973), parameterizing the kinematic viscosity as $\nu = \alpha c_s H$, where c_s is the sound speed and H is the height above the midplane (Pringle 1981). For an $\alpha-$disk, the self-similar solution for the surface density Σ is given by (Lynden-Bell & Pringle 1974; Hartmann et al. 1998)

$$\Sigma_{\rm gas}(R) = \frac{(2-\gamma)\, M_{\rm disk}(t)}{2\pi R_{\rm c}(t)^2} \left(\frac{R}{R_{\rm c}(t)}\right)^{-\gamma} \exp\left[-\left(\frac{R}{R_{\rm c}(t)}\right)^{2-\gamma}\right], \tag{4.1}$$

where γ is set by assuming that the viscosity varies radially as $\nu \propto R^\gamma$ and $M_{\rm disk}$ and $R_{\rm c}$ are the disk mass and the characteristic radius, respectively.

Following Hartmann et al. (1998), the time evolution of $M_{\rm disk}$ and $R_{\rm c}$ is described by

$$M_{\rm disk}(t) = M_{\rm disk}(t=0)\left(1+\frac{t}{t_{\rm visc}}\right)^{-\frac{1}{[2(2-\gamma)]}} = M_{\rm init}\left(1+\frac{t}{t_{\rm visc}}\right)^{-\frac{1}{2}} \tag{4.2}$$

$$R_{\rm c}(t) = R_{\rm c}(t=0)\left(1+\frac{t}{t_{\rm visc}}\right)^{\frac{1}{(2-\gamma)}} = R_{\rm init}\left(1+\frac{t}{t_{\rm visc}}\right), \tag{4.3}$$

where $t_{\rm visc}$ is the viscous timescale and we defined short hands for the initial disk mass $M_{\rm init} \equiv M_{\rm disk}(t=0)$, the initial characteristic size $R_{\rm init} \equiv R_{\rm c}(t=0)$. For the second step and the rest of this work, we assumed $\gamma = 1$ since for a typical temperature profile it corresponds to the case of a constant $\alpha_{\rm visc}$.

Combining equations (4.1), (4.2), and (3) we obtain the time evolution of the surface density profile

$$\Sigma_{\rm gas}(t,R) = \frac{M_{\rm disk}(t)}{2\pi R_{\rm c}(t)^2}\left(\frac{R}{R_{\rm c}(t)}\right)^{-1}\exp\left[-\left(\frac{R}{R_{\rm c}(t)}\right)\right] \tag{4.4}$$

$$= \frac{M_{\rm init}}{2\pi R_{\rm init}^2}\left(1+\frac{t}{t_{\rm visc}}\right)^{-\frac{3}{2}}\left(\frac{R}{R_{\rm init}\left(1+\frac{t}{t_{\rm visc}}\right)}\right)^{-1} \tag{4.5}$$

$$\times \exp\left[-\left(\frac{R}{R_{\rm init}\left(1+\frac{t}{t_{\rm visc}}\right)}\right)\right]. \tag{4.6}$$

4.2.2 Initial conditions of the models

For a viscous disk the initial disk mass $M_{\rm init}$ is related to the stellar accretion rate through (Hartmann et al. 1998)

$$M_{\rm init} = 2t_{\rm visc}\dot{M}_{\rm acc}(t)\left(\frac{t}{t_{\rm visc}}+1\right)^{3/2}. \tag{4.7}$$

Under the assumption that the disk evolved viscously, we calculated $M_{\rm init}$ given the stellar accretion rate measured at a time t and the viscous timescale of the disk. For various star-forming regions, for example, Lupus and Chamaeleon I, stellar accretion rates were determined from observations (see, e.g. Alcalá et al. 2014, 2017; Manara et al. 2017). A correlation was found between the stellar mass M_* and the stellar accretion rate $\dot{M}_{\rm acc}$, best described by a broken power law. Based on equation (4.7) a disk around a more massive star therefore has a higher initial disk mass for the same viscous timescale.

For our models we considered three stellar masses: $0.1, 0.32,$ and 1.0 $M_\odot$. For each stellar mass, we used the observations, presented in Figure 6 of Alcalá et al. (2017), to pick the average stellar accretion rate associated with that stellar mass. For each stellar accretion rate, we calculated the initial disk mass using equation (4.7) for three different viscous timescales. The viscous timescale is computed for three values of the dimensionless viscosity $\alpha_{\rm visc} = 10^{-2}, 10^{-3}, 10^{-4}$, assuming a characteristic radius of 10 AU (which is the radius we employed; see below) and a disk temperature $T_{\rm disk}$ of 20 K (see, e.g. equation 37 in Hartmann et al. 1998)

$$\frac{t_{\rm visc}}{\rm yr} = \frac{R_{\rm c}^2}{\nu} \simeq 8\times10^4\left(\frac{\alpha_{\rm visc}}{10^{-2}}\right)^{-1}\left(\frac{R_{\rm c}}{10\ {\rm AU}}\right)\left(\frac{M_*}{0.5\ M_\odot}\right)^{1/2}\left(\frac{T_{\rm disk}}{10\ {\rm K}}\right)^{-1}. \tag{4.8}$$

The combination of three stellar accretion rates and three viscous timescales results in nine different disk models (see Table 4.1). Figure 4.1 shows how disk parameters such as $\dot{M}_{\rm acc}$, $R_{\rm c}$, and $M_{\rm disk}$ evolve with time for the models with $M_* = 0.1$ $M_\odot$. Similarly, Figure 4.9 shows how $M_{\rm disk}$ evolves for the models with $M_* = 0.32$ $M_\odot$ and

1.0 $M_\odot$. We note that the trends for $M_{\rm disk}$(t) are very similar, apart from starting at a higher initial $M_{\rm disk}$ ($\sim 10^{-2}$ $M_\odot$ for $M_* = 0.32$ $M_\odot$ and $\sim 10^{-1}$ $M_\odot$ for $M_* = 1.0$ $M_\odot$; cf. Table 4.1).

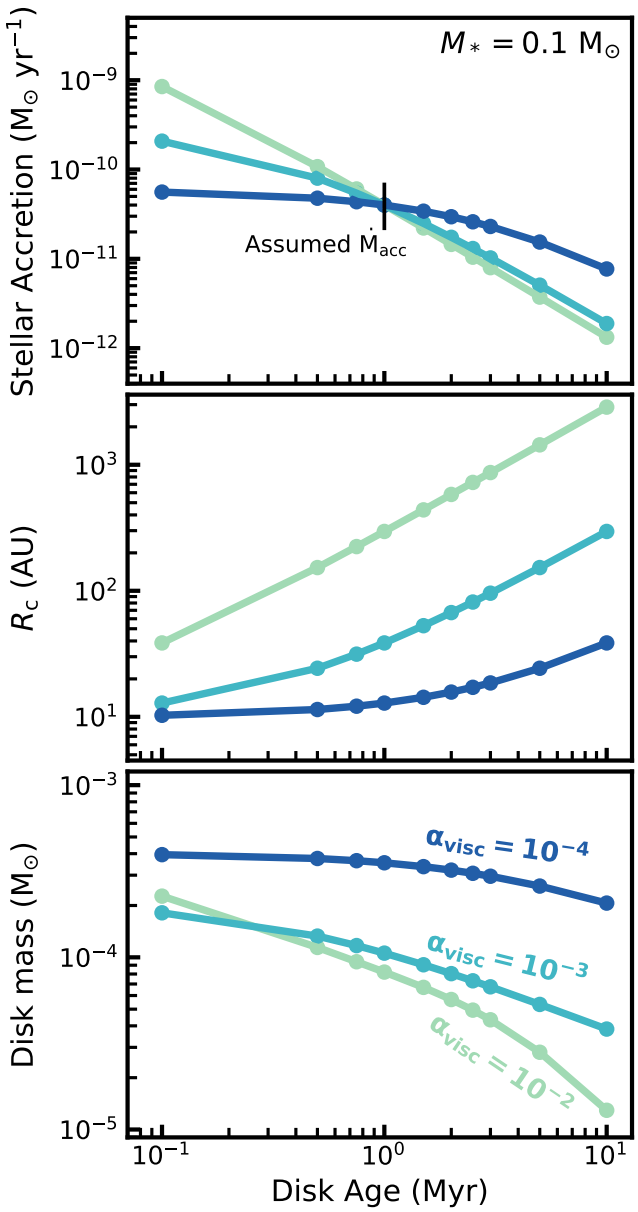

Figure 4.1: Evolution of the disk parameters for the models with $M_* = 0.1$ $M_\odot$. The colors show different $\alpha_{\rm visc}$. For reference, the viscous timescales are 0.046, 0.46, and 4.6 Myr for $\alpha_{\rm visc} = 10^{-2}, 10^{-3}$, and 10^{-4}, respectively. The evolution of the disk mass for the models with $M_* = 0.32$ $M_\odot$ and 1.0 $M_\odot$ is shown Figure 4.9. For the model with $\alpha_{\rm visc} = 10^{-2}$, $M_{\rm disk}$ starts out at higher mass compared to the model with $\alpha_{\rm visc} = 10^{-3}$, but this model also loses mass at a faster rate.

The initial size of disks is less well constrained, predominately because of a lack of high-resolution observations for younger Class 1 and 0 objects. Recently, Tobin et al. 2020 present the VANDAM II survey: 330 protostars in Orion observed at 0.87 millimeter with ALMA at a resolution of $\sim 0\farcs1$ ($\sim$ 40 AU in diameter). By fitting a 2D Gaussian to their dust millimeter observations, the authors determined median dust disk radii of $44.9^{+5.8}_{-3.4}$ AU and $37.0^{+4.9}_{-3.0}$ AU for their Class 0 and Class 1 protostars, suggesting that the majority of disks are initially very compact. It should be noted that it is unclear whether the extent of the dust emission can be directly related to the gas disk size. However, there is also similar evidence from the gas that Class 1 and 0 objects are compact. As part of the CALYPSO large program, Maret et al. (2020) observed 16 Class 0 protostars and found that only two sources show Keplerian rotation at $\sim$ 50 AU scales, suggesting that Keplerian disks larger than 50 AU, such as found for VLA 1623 (Murillo et al. 2013), are uncommon. We therefore adopted an initial disk size of $R_{\rm init}$ = 10 AU for our models. In Section 4.4.2 we discuss the impact of this choice.

Table 4.1: Initial conditions of our `DALI` models

M_*	($M_\odot$)	0.1	0.32	1.0
$\dot{M}_{\rm acc}$	($M_\odot$ yr^{-1})	4×10^{-11}	2×10^{-9}	1×10^{-8}
		$\alpha_{\rm visc} = 10^{-2}$		
$t_{\rm visc}$	($\times 10^6$ yr)	0.035	0.046	0.115
$M_{\rm init}$	($M_\odot$)	4.5×10^{-4}	1.99×10^{-2}	6.9×10^{-2}
		$\alpha_{\rm visc} = 10^{-3}$		
$t_{\rm visc}$	($\times 10^6$ yr)	0.35	0.46	1.15
$M_{\rm init}$	($M_\odot$)	2.1×10^{-4}	1.0×10^{-2}	5.9×10^{-2}
		$\alpha_{\rm visc} = 10^{-4}$		
$t_{\rm visc}$	($\times 10^6$ yr)	3.5	4.6	11.5
$M_{\rm init}$	($M_\odot$)	4.1×10^{-4}	2.5×10^{-2}	2.6×10^{-1}

4.2.3 `DALI` models

Based on our nine sets of initial conditions, we calculated $M_{\rm disk}$ and $R_{\rm c}$ at ten disk ages between 0.1 and 10 Myr using equations (4.2) and (3) (see Figure 4.1 for an example). From $M_{\rm disk}$(t) and $R_{\rm c}$(t), we calculated $\Sigma_{\rm gas}$(t) and used that as input for the thermochemical code `DALI` (Bruderer et al. 2012; Bruderer 2013). Based on a 2D physical disk structure, `DALI` calculates the thermal and chemical structure of the disk self-consistently. First, the dust temperature structure and the internal radiation field are computed using a 2D Monte Carlo method to solve the radiative transfer equation. In order to find a self-consistent solution, the code iteratively solves the time-dependent chemistry, calculates molecular and atomic excitation levels, and computes the gas temperature by balancing heating and cooling processes. The model can then be ray traced to construct synthetic emission maps. A more detailed description of the code is provided in Appendix A of Bruderer et al. (2012).

For the vertical structure of our models we assumed a Gaussian density distribution,

with a radially increasing scale height of the form $h = h_c\,(R/R_c)^{\psi}$. In this equation, h_c is the scale height at R_c and ψ is the flaring angle. The stellar spectrum used in our models is a black body with $T_{\rm eff} = 4000$ K. To this black body we added excess UV radiation, resulting from accretion, in the form of 10000 K black body. For the luminosity of this component, we assume that the gravitational potential energy of the accreted mass is released with 100% efficiency (see, e.g. Kama et al. 2015). For the external UV radiation we assumed a standard interstellar radiation field of 1 G_0 (Habing 1968)). These parameters are summarized in Table 4.2.

Table 4.2: Fixed `DALI` parameters of the physical model.

Parameter	Range
Chemistry	
Chemical age	0.1-10*,† Myr
[C]/[H]	$1.35 \cdot 10^{-4}$
[O]/[H]	$2.88 \cdot 10^{-4}$
Physical structure	
γ	1.0
ψ	0.15
h_c	0.1
R_c	$10 - 3 \times 10^{3,\dagger}$ AU
$M_{\rm gas}$	$10^{-5} - 10^{-1,\dagger}$ $M_\odot$
Gas-to-dust ratio	100
Dust properties	
$f_{\rm large}$	0.9
χ	0.2
composition	standard ISM[1]
Stellar spectrum	
$T_{\rm eff}$	4000 K + Accretion UV
L_*	0.28 $L_\odot$
$\zeta_{\rm cr}$	10^{-17} s^{-1}
Observational geometry	
i	0°
PA	0°
d	150 pc

Notes. *The age of the disk is taken into account when running the time-dependent chemistry. †These parameters evolve with time (see Figure 4.1 and Sect. 4.4.3). [1]Weingartner & Draine 2001, see also Section 2.5 in Facchini et al. 2017.

In our models we included the effects of dust settling by subdividing our grains into two populations. A population of small grains (0.005-1 μm) follows the gas density distribution both radially and vertically. A second population of large grains (1-10^3 μm), making up 90% of the dust by mass, follows the gas radially but has its scale height reduced by a factor $\chi = 0.2$ with respect to the gas. We computed the dust opacities for both populations using a standard interstellar medium (ISM) dust composition following Weingartner & Draine (2001), with a Mathis-Rumpl-Nordsieck (MRN) (Mathis et al. 1977) grain size distribution. We did not include any radial

drift or radially varying grain growth in our DALI models (cf. Facchini et al. 2017). However, we note that Trapman et al. (2019) show that dust evolution does not affected measured gas outer radii.

4.3 Results

4.3.1 Time evolution of the ^{12}CO emission profile

To first order, the evolution of ^{12}CO intensity profile is determined by three time-dependent processes as follows:

1. Viscous spreading moves material, including CO, to larger radii resulting in more extended CO emission.

2. The disk mass decreases with time, lowering surface density, which in the outer disk allows CO to be more easily photodissociated. This removes CO from the outer disk and lowers the CO flux coming from these regions.

3. Over longer timescales, time-dependent chemistry results in CO being converted into CH_4, CO_2, and CH_3OH. This is discussed separately in more detail in Section 4.4.3.

The combined effect of the first two processes on the ^{12}CO emission profile can be seen in Figure 4.2 for disks with a stellar mass of $M_* = 0.1$ M$_\odot$. Similar profiles for the remaining disks are shown in Figure 4.12

For a high $\alpha_{\rm visc}$ of 0.01 the viscous timescale is short compared to the disk age and viscous evolution is happening fast. This is reflected in the ^{12}CO emission, which spreads quickly (within 1 Myr) from $\sim$ 200 AU to $\sim$ 400 AU. After $\sim$ 2 Myr the ^{12}CO emission in the outer parts of the disk starts to decrease. At this point the total column densities in the outer disk are low enough that CO is removed through photodissociation. As a reference, by 2 Myr the disk mass of the models has dropped to $M_{\rm disk} = 5 \times 10^{-5}$ M$_\odot$ and its characteristic size has increased to $R_{\rm c} = 400$ AU (see Figure 4.1).

For models with $\alpha_{\rm visc} = 10^{-3}$, shown in the middle panel of Figure 4.2, viscous spreading of the disk dominates the evolution of the ^{12}CO emission profile. Compared to the $\alpha_{\rm visc} = 10^{-2}$ models the column density in the outer disk never becomes low enough for CO to be efficiently photodissociated.

The models with $\alpha_{\rm visc} = 10^{-4}$, presented in the right panel of Figure 4.2, shows only small changes in the emission profile. For these models the viscous timescale is $\sim$ 3.5 Myr, meaning that within the 10 Myr lifetime considered the surface density does not go through much viscous evolution.

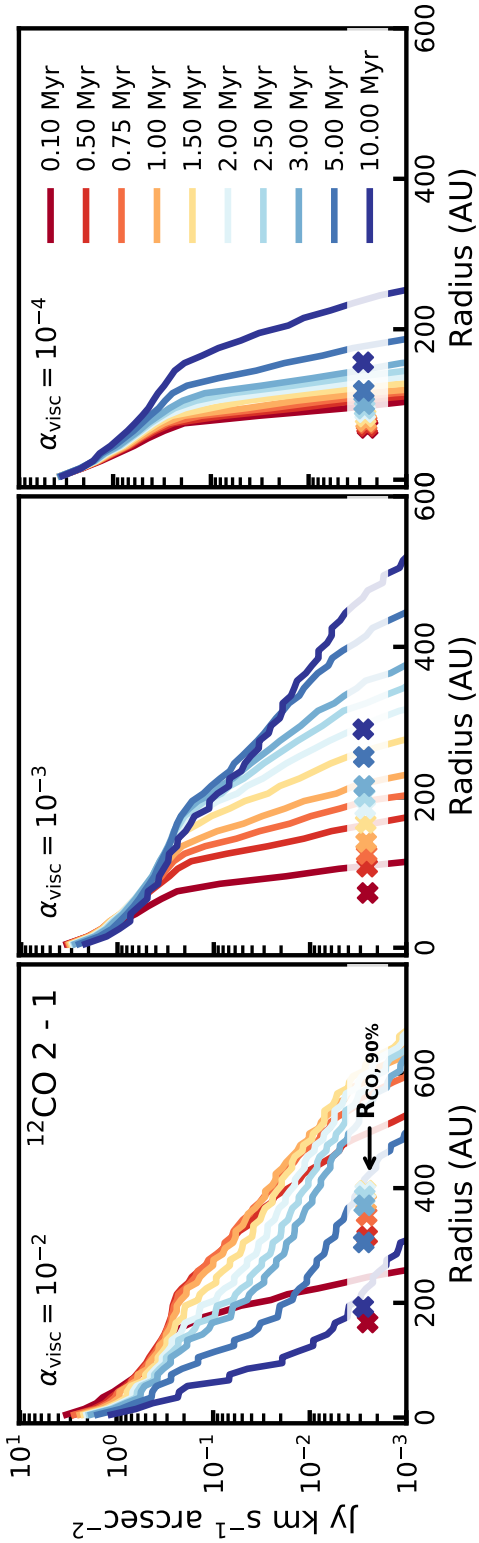

Figure 4.2: Evolution of the ^{12}CO 2 - 1 radial intensity profiles for models with $M_* = 0.1$ $M_\odot$. The colors indicate various disk ages between 0.1 and 10 Myr. The crosses at the bottom of each panel show the gas outer radius, defined as the radius that encloses 90% of the total ^{12}CO 2 - 1 flux.

4.3.2 Evolution of the observed gas outer radius

From the ^{12}CO emission maps we can calculate the outer radius that would be obtained from observations. We define the observed gas outer radius, $R_{\rm CO,\ 90\%}$, as the radius that encloses 90% of the total ^{12}CO flux. A gas outer radius defined this way encloses most (> 98%) of the disk mass and traces a fixed surface density in the outer disk (Trapman et al. 2019). We note that we do not include observational factors, such as noise, which affect the $R_{\rm CO,\ 90\%}$ that is measured. To accurately retrieve $R_{\rm CO,\ 90\%}$ from observations requires a peak S/N > 10 on the moment zero map of the ^{12}CO emission (cf. Trapman et al. 2019). The radii discussed in this work are measured from ^{12}CO $J = 2 - 1$ emission, but tests show that gas outer radii measured from ^{12}CO $J = 3 - 2$ are the same to within a few percent.

Figure 4.3 shows how the observed outer radius changes as a result of viscous evolution. The top panel shows $R_{\rm CO,\ 90\%}$ for models with $M_* = 0.1$ M$_\odot$. For $\alpha_{\rm visc} = 10^{-2}$ the gas outer radius first increases until it starts to decrease at ~ 2 Myr. The decrease in $R_{\rm CO,\ 90\%}$ is due to decreasing column densities in the outer disk, allowing CO to be more easily photodissociated (for details, see Section 4.3.1). For $\alpha_{\rm visc} = 10^{-3}$, $R_{\rm CO,\ 90\%}$ increases monotonically from ~ 70 AU to ~ 280 AU. The trend is similar for $\alpha_{\rm visc} = 10^{-4}$ but $R_{\rm CO,\ 90\%}$ increases at a slower rate, ending up at $R_{\rm CO,\ 90\%} \sim 150$ AU after 10 Myr.

For models with $M_* = 0.32$ M$_\odot$ and 1.0 M$_\odot$, the initial and final disk masses are much higher compared to the models with $M_* = 0.1$ M$_\odot$. As a result, photodissociation does not have a significant effect on $R_{\rm CO,\ 90\%}$ and $R_{\rm CO,\ 90\%}$ does not significantly decrease with age. In addition, the disk sizes for these two groups of models are very similar. For $\alpha_{\rm visc} = 10^{-2}$, $R_{\rm CO,\ 90\%}$ instead rapidly increases from $\sim 180 - 250$ AU at 0.1 Myr to $1500 - 1800$ AU at 10 Myr. For $\alpha_{\rm visc} = 10^{-3}$ the growth of $R_{\rm CO,\ 90\%}$ is less extreme in comparison, but observed disk sizes still reach $500 - 700$ AU after 10 Myr. Owing to the long viscous timescales of $5 - 10$ Myr for the models with $\alpha_{\rm visc} = 10^{-4}$, $R_{\rm CO,\ 90\%}$ does not increase significantly (i.e., by less than a factor of ~ 2) over a disk lifetime of ~ 10 Myr.

For more embedded star-forming regions, the ^{12}CO emission from the disk can be contaminated by the cloud, either by having ^{12}CO emission from the cloud mixed in with the emission from the disk or through cloud material along the line of sight absorbing the ^{12}CO emission from the disk. This can prevent using ^{12}CO to accurately measure disk sizes. We therefore also examined disk sizes measured using 90% of the ^{13}CO 2-1 flux, which are shown in Figure 4.14. Apart from being a factor $\sim 1.4 - 2$ smaller than the ^{12}CO outer radii, the ^{13}CO outer radii evolve similarly as $R_{\rm CO,\ 90\%}$. The ^{13}CO outer radii are smaller than $R_{\rm CO,\ 90\%}$ because the less abundant ^{13}CO is more easily removed in the outer parts of the disk through photodissociation. Our conclusions for $R_{\rm CO,\ 90\%}$ are therefore also applicable for gas disk sizes measured from ^{13}CO emission. However, see Section 4.4.3 on how chemical depletion of CO through grain-surface chemistry affects this picture.

Overall we find that the observed outer radius increases with time and is larger for a disk with a higher $\alpha_{\rm visc}$. The exception to this rule are the models with low stellar mass ($M_* = 0.1$ M$_\odot$) and high viscosity ($\alpha_{\rm visc} = 10^{-2}$). These highlight the caveat that if the disk mass becomes too low, CO becomes photodissociated in the outer disk and the observed outer radius decreases with time.

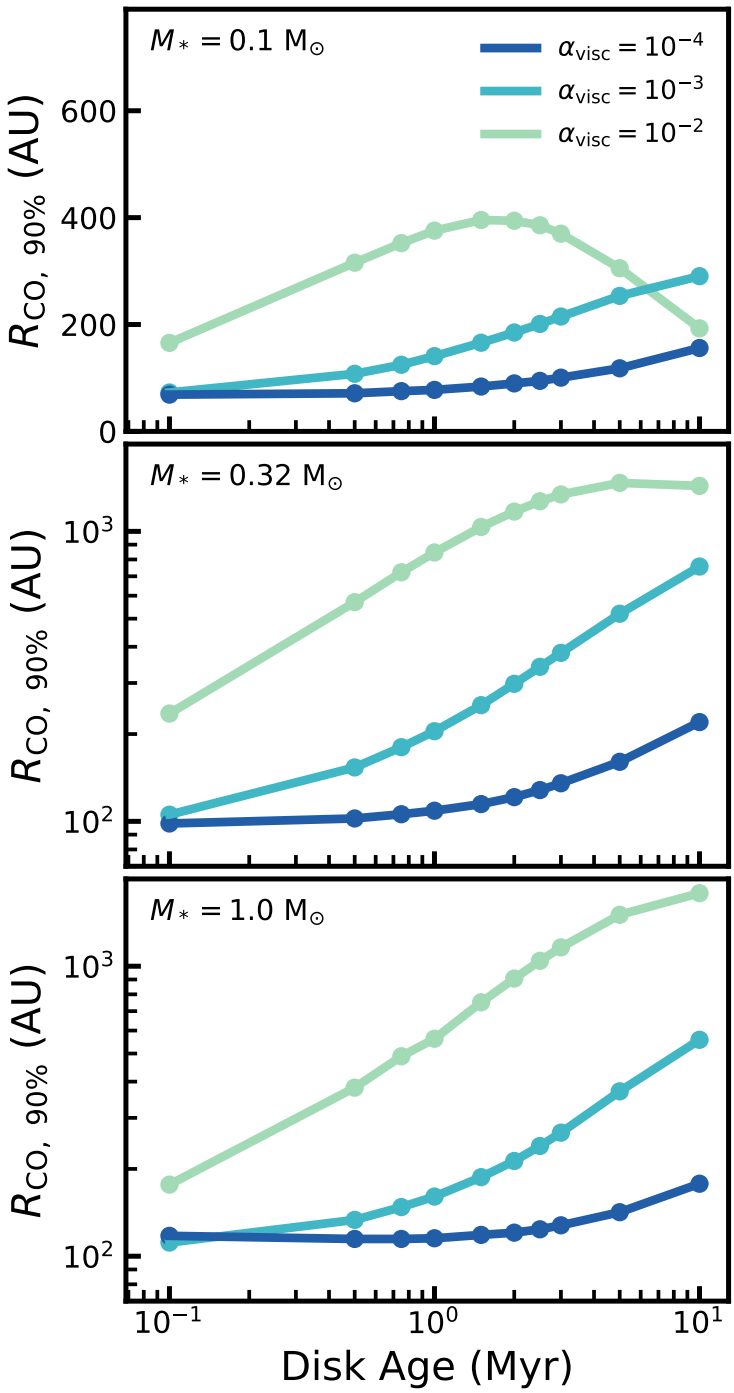

Figure 4.3: Gas outer radius vs. disk age, defined as the radius that encloses 90% of the ^{12}CO 2-1 flux. The top, middle, and bottom panels show models with various stellar masses (cf. Table 4.1). The colors correspond to the α_{visc} of the model.

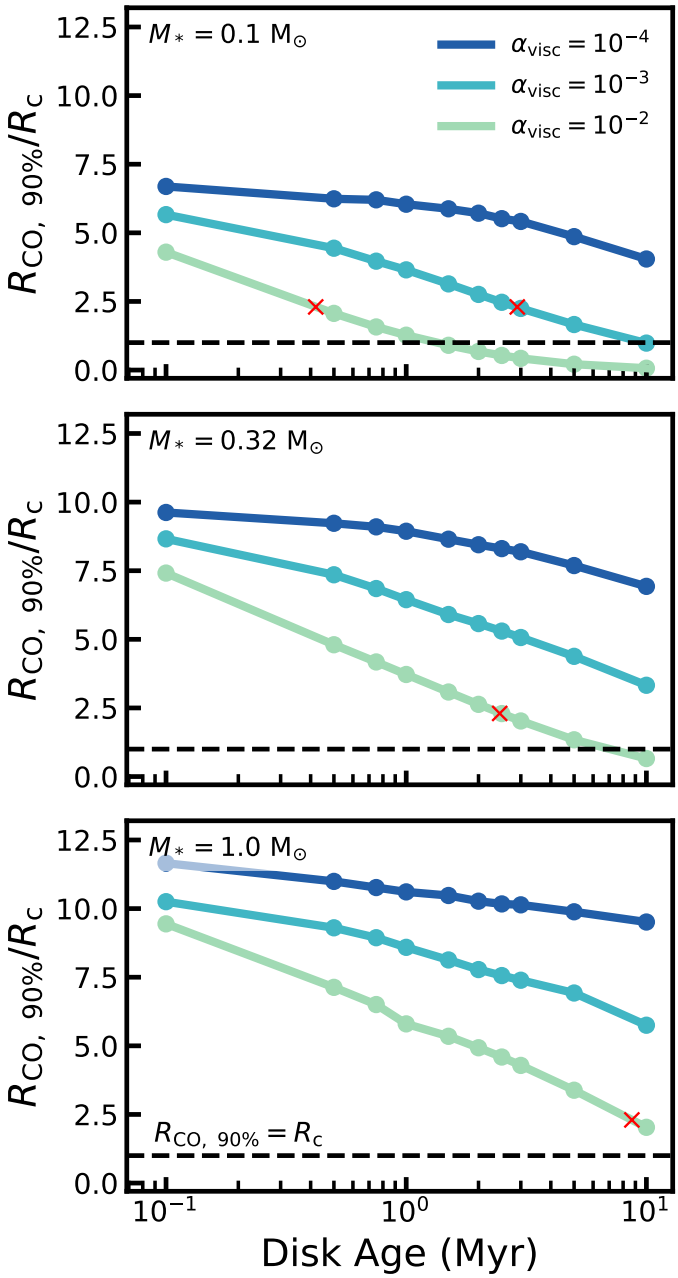

Figure 4.4: Ratio of gas outer radius over characteristic radius vs. disk age. The black dashed line shows where $R_{CO,\ 90\%} = R_c$. The top, middle, and bottom panels show models with various stellar masses (cf. Table 4.1). The colors correspond to the α_{visc} of the model. The red crosses denote where $R_{CO,\ 90\%}/R_c = 2.3$, that is, where $R_{CO,\ 90\%}$ encloses 90% of the total disk mass (see Section 4.3.4)

4.3.3 Gas outer radius traces viscous evolution

The previous section has shown that disks with higher $\alpha_{\rm visc}$, which evolve over a shorter viscous timescale, are overall larger at a given disk age. To quantify this, it is worthwhile to examine how well the observed gas outer radius $R_{\rm CO,\ 90\%}$ traces the characteristic size $R_{\rm c}$ of the disk.

Figure 4.4 shows the ratio $R_{\rm CO,\ 90\%}/R_{\rm c}$ as a function of disk age for the three sets of stellar masses. If $R_{\rm CO,\ 90\%}$ were only affected by viscous spreading it would grow at the same rate as the characteristic radius, $R_{\rm CO,\ 90\%} \propto R_{\rm c}$, represented by a horizontal line in Figure 4.4. Instead we see $R_{\rm CO,\ 90\%}/R_{\rm c}$ decreasing with disk age, indicating that the observed outer radius grows at a slower rate than the viscous spreading of the disk. The main cause for the slower growth rate of $R_{\rm CO,\ 90\%}$ is the decreasing disk mass over time because $R_{\rm CO,\ 90\%}$ traces a fixed surface density. As shown in Trapman et al. (2019), $R_{\rm CO,\ 90\%}$ coincides with the location in the outer disk, where CO is no longer able to effectively self-shield against photodissociation and is quickly removed from the gas. The CO column density threshold for CO to self-shield is $N_{\rm CO} \geq 10^{15}$ cm^{-2} (van Dishoeck & Black 1988). Thus, given that $R_{\rm CO,\ 90\%}$ traces a point of fixed column density, it scales with the total disk mass. As a result of angular momentum transport via viscous stresses, material is accreted onto the star, causing the total disk mass to decrease following equation (4.2) (see, e.g, Figure 4.1), which limits the growth of $R_{\rm CO,\ 90\%}$.

Figure 4.4 also shows that $R_{\rm CO,\ 90\%}/R_{\rm c}$ is larger for models with a lower $\alpha_{\rm visc}$; this difference becomes larger for older disks. This behavior can also be related to disk mass. As shown in Figure 4.1 disk models with a lower $\alpha_{\rm visc}$ have a higher disk mass. For the same $R_{\rm c}$ a higher disk mass, to first order, results in higher CO column densities in the outer disk. As a result CO is able to self-shield against photodissociation further out in the disk, increasing the difference between $R_{\rm CO,\ 90\%}$ and $R_{\rm c}$.

In conclusion, we find that $R_{\rm CO,\ 90\%}/R_{\rm c}$ is between 0.1 and 12 and is mainly determined by the time evolution of the disk mass, which is set by the assumed viscosity. To infer $R_{\rm c}$ directly from $R_{\rm CO,\ 90\%}$ requires information on the total disk gas mass.

4.3.4 Possibility of measuring $\alpha_{\rm visc}$ from observed $R_{\rm CO,\ 90\%}$

A useful definition for an outer radius of a disk is that it encloses most of the mass in the disk. In this case, using a few simple assumptions, we can relate the outer radius directly to $\alpha_{\rm visc}$. If we assume that the viscous timescale at the outer radius of the disk, given by $t_{\rm visc} \approx R_{\rm out}^2 \nu^{-1}$, is approximately equal to the age of the disk, given by $\dot{M}_{\rm acc} \approx M_{\rm disk}/t_{\rm visc}$, we can write $\alpha_{\rm visc}$ as (see, e.g. Hartmann et al. 1998; Jones et al. 2012; Rosotti et al. 2017)

$$\alpha_{\rm visc} = \frac{\dot{M}_{\rm acc}}{M_{\rm disk}} \cdot c_s^{-2} \cdot \Omega_K \cdot R_{\rm out}^2, \tag{4.9}$$

where $\dot{M}_{\rm acc}$ is the stellar accretion rate, $M_{\rm disk}$ is the total disk mass, c_s is the sound speed, Ω_K is the Keplerian orbital frequency, and $R_{\rm out}$ is the physical outer radius of the disk.

In absence of this physical outer radius, Ansdell et al. (2018) used the observed gas outer radius $R_{\rm CO,\ 90\%}$, based on the ^{12}CO 2-1 emission, to measure $\alpha_{\rm visc}$ for 17 disks in Lupus finding a wide range of $\alpha_{\rm visc}$, spanning two orders of magnitude between 3×10^{-4} and 0.09.

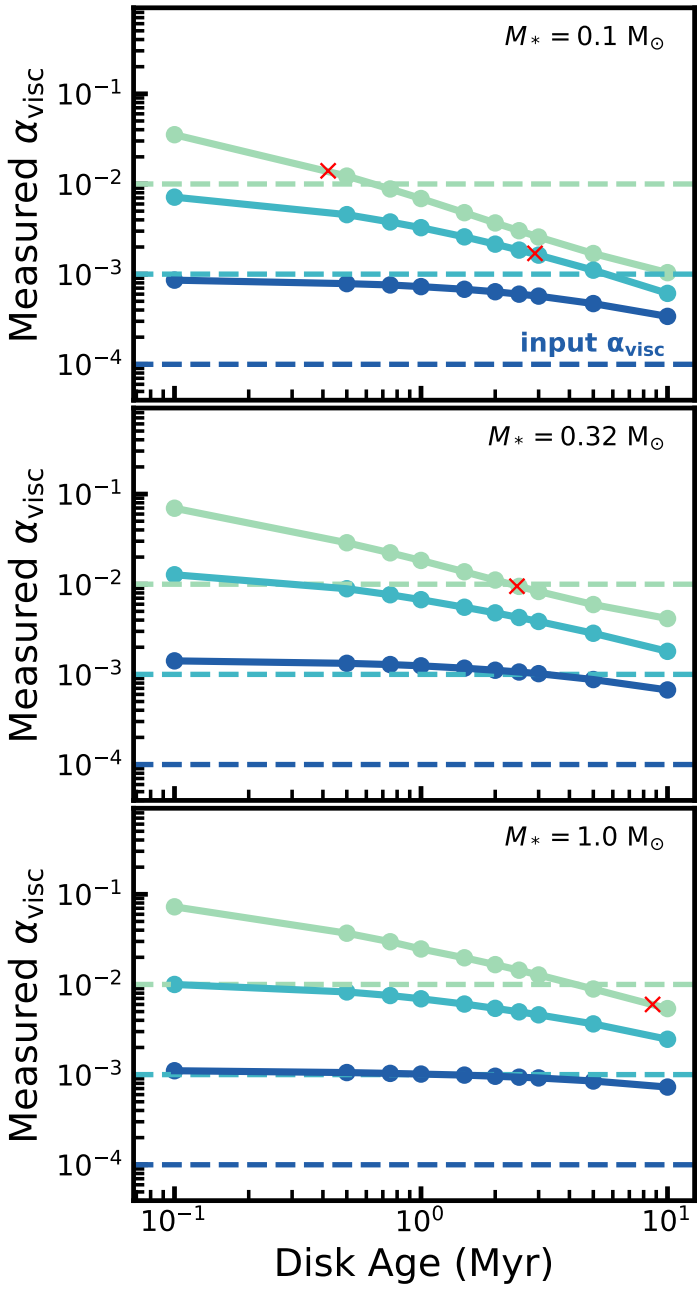

Figure 4.5: Comparison between $\alpha_{\rm visc}$ measured from $R_{\rm CO,\ 90\%}$ (solid line) and the input $\alpha_{\rm visc}$ (dashed line). The colors correspond to the input $\alpha_{\rm visc}$ of the model. The top, middle, and bottom panels show models with different stellar masses (cf. Table 4.1). The red crosses denote where $R_{\rm CO,\ 90\%}/R_{\rm c} = 2.3$ and $R_{\rm CO,\ 90\%}$ encloses 90% of $M_{\rm disk}$ (cf. Section 4.3.4 and Figure 4.4). The red crosses denote where $R_{\rm CO,\ 90\%}/R_{\rm c} = 2.3$, that is, where $R_{\rm CO,\ 90\%}$ encloses 90% of the total disk mass (see Section 4.3.4).

For our models we have both $R_{\rm CO,\ 90\%}$, measured from our models, and input $\alpha_{\rm visc}$, thus we can examine how well $\alpha_{\rm visc}$ can be retrieved from the observed gas outer radius $R_{\rm CO,\ 90\%}$. As we are mainly interested in the correlation between $\alpha_{\rm visc}$ and $R_{\rm CO,\ 90\%}$, we assume that M_*, $\dot{M}_{\rm acc}$, and $M_{\rm disk}$ are known, and c_s is calculated assuming a disk temperature of 20 K, which is the same temperature used to calculate $t_{\rm visc}$ in Section 4.2.2.

Figure 4.5 shows $\alpha_{\rm visc}$ measured using $R_{\rm CO,\ 90\%}$, for our models and compares this value to the $\alpha_{\rm visc}$ that was used as input for the models. For all disk models the measured $\alpha_{\rm visc}$ decreases with age and, for most ages, we find $\alpha_{\rm visc}$(measured) > $\alpha_{\rm visc}$(input). Both of these observations can be traced back to which radius is used in Equation (4.9) to calculate $\alpha_{\rm visc}$(measured). In the assumptions going into deriving Equation (4.9), $R_{\rm out}$ is defined as the radius that encloses all (100 %) of the mass of the disk. In our models in which the surface density follows a tapered power law the radius that encloses 100 % of the mass is infinite, but we can instead take $R_{\rm out}$ as a radius that encloses a large, fixed fraction of the disk mass. For a tapered power law, this $R_{\rm out}$ is directly related to $R_{\rm c}$. As an example, for a tapered power law where $\gamma = 1$, the radius that encloses 90% of the disk mass is $2.3 \times R_{\rm c}$. For $R_{\rm out} = 2.3 \times R_{\rm c}$ in Equation (4.9) we obtain approximately the same $\alpha_{\rm visc}$ that was put into the model. Ideally we would therefore like $R_{\rm CO,\ 90\%}$ to also enclose a large, fixed fraction of the disk mass, or continuing our example, we would like $R_{\rm CO,\ 90\%} \approx 2.3 \times R_{\rm c}$, independent of disk age and mass. However, in Section 4.3.3 we show that $R_{\rm CO,\ 90\%}/R_{\rm c}$ lies between 0.1 and 10 and decreases with disk age. Figure 4.4 shows that $R_{\rm CO,\ 90\%}/R_{\rm c} \gg 2.3$ for most disk ages, leading us to overestimate $\alpha_{\rm visc}$ when measured from $R_{\rm CO,\ 90\%}$. Taking the example discussed before, if we compare Figures 4.5 and 4.4 we find that at disk ages where $R_{\rm CO,\ 90\%}/R_{\rm c} \approx 2.3$ our $\alpha_{\rm visc}$ measured from $R_{\rm CO,\ 90\%}$ is within a factor of 2 of the input $\alpha_{\rm visc}$.

Summarizing we find that in most cases, $R_{\rm CO,\ 90\%}/R_{\rm c} \gg 2.3$ and we measure an $\alpha_{\rm visc}$ much larger than the input $\alpha_{\rm visc}$, up to an order of magnitude higher, especially if the input $\alpha_{\rm visc}$ is low. Given that at 1 Myr the measured $\alpha_{\rm visc}$ is $5 - 10\times$ larger than the input $\alpha_{\rm visc}$, this implies that the $\alpha_{\rm visc}$ determined by Ansdell et al. (2018) likely overestimates the true $\alpha_{\rm visc}$ of the disks in Lupus by a factor 5-10.

4.4 Discussion

4.4.1 Comparing to observations

Gas disk sizes have now been measured consistently for a significant number of disks. In contrast with Najita & Bergin (2018), in this paper we chose to select homogeneous samples (in terms of analysis and tracer). These samples are Ansdell et al. (2018) and Barenfeld et al. (2017), who measured $R_{\rm CO,\ 90\%}$ for 22 sources in Lupus and 7 sources in Upper Sco. Between them, these disks span between 0.5 and 11 Myr in disk ages. In Figure 4.6 we compare our models to these observations, where sources with $M_* \leq 0.66$ $M_\odot$ are compared to models with $M_* = 0.32$ $M_\odot$ and those with $M_* > 0.66$ $M_\odot$ are compared to models with $M_* = 1.0$ $M_\odot$. Ansdell et al. (2018) define the gas outer radius as the radius that encloses 90% of the ^{12}CO 2 - 1 emission, so we take their values directly. For the disks in Upper Sco we calculate $R_{\rm CO,\ 90\%}$ from their fit to the observed ^{12}CO intensity (cf. Barenfeld et al. 2017). Stellar ages and masses were determined by comparing pre-main-sequence evolutionary models

to X-shooter observations of these sources (Alcalá et al. 2014, 2017). Lacking such observations for Upper Sco, we instead use the 5-11 Myr stellar age of Upper Sco (see, e.g. Preibisch et al. 2002; Pecaut et al. 2012) for all sources in this region. The observations are summarized in Table 4.3.

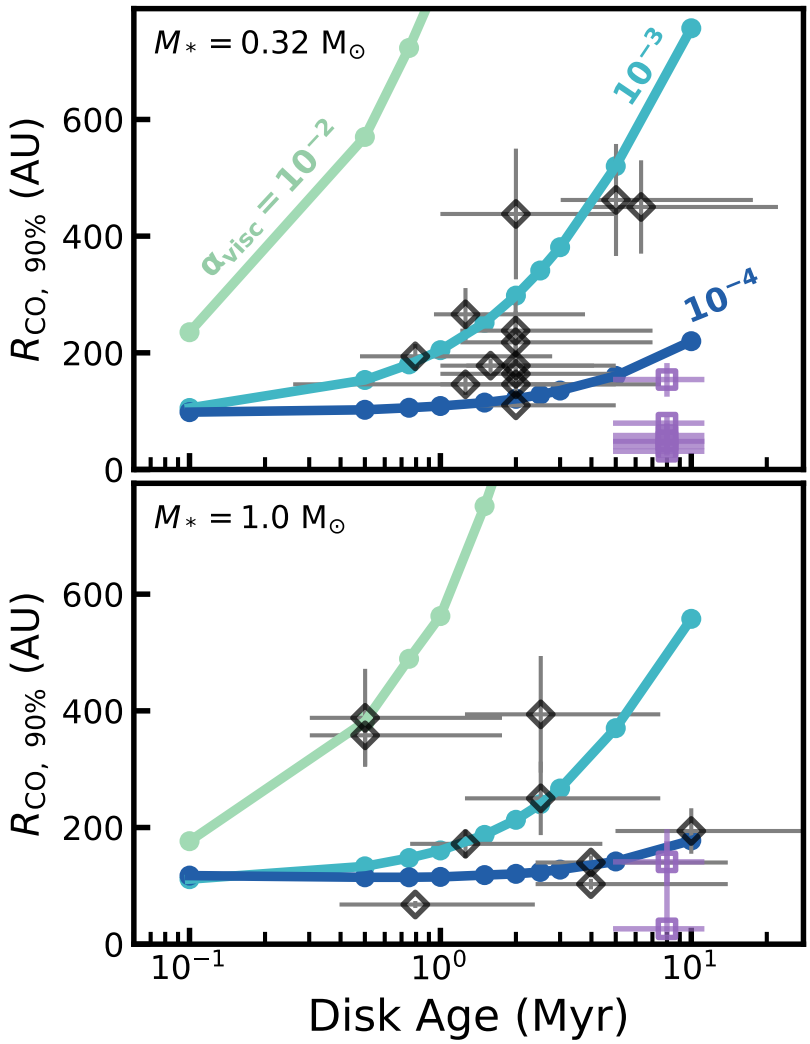

Figure 4.6: Gas outer radii of our models ($R_{\mathrm{CO,\ 90\%}}$) compared to observations. The colors correspond to the α_{visc} of the model. The black open diamonds show observed gas outer radii in Lupus (Ansdell et al. 2018) and the purple open squares denote observed gas outer radii in Upper Sco (Barenfeld et al. 2017). The Upper Sco outer radii shown are 90% outer radii, calculated from their fit to the observed ^{12}CO intensity. The top and bottom panels split models and observations based on stellar mass. The sources with $M_* \leq 0.66$ M$_\odot$ are compared to models with $M_* = 0.32$ M$_\odot$; those with $M_* > 0.66$ M$_\odot$ are compared to models with $M_* = 1.0$ M$_\odot$. Only panels for $M_* = 0.32$ and 1.0 M$_\odot$ are shown because the sample of observations considered in this work does not contain any objects with $M_* \sim 0.1$ M$_\odot$.

As shown in Figure 4.6, most of the Lupus observations lie between the models with $\alpha_{\rm visc} = 10^{-3}$ and $\alpha_{\rm visc} = 10^{-4}$. Most of the disks can therefore been explained as viscously spreading disks with $\alpha_{\rm visc} = 10^{-4}-10^{-3}$ that start out small ($R_{\rm init} = 10$ AU). Only two sources with $M_* = 1.0$ M$_\odot$, IM Lup and Sz 98 (also known as HK Lup), require a larger $\alpha_{\rm visc} \simeq 10^{-2}$ to explain the observed gas disk size given their age.

It is interesting to note that Lodato et al. (2017) reached a similar conclusion using a completely different method. They show that a simple viscous model can reproduce the observed relation between stellar mass accretion and disk mass in Lupus (see Manara et al. 2016a). To match both the average disk lifetime and the observed scatter in the $\dot{M}_{\rm acc}$-$M_{\rm disk}$ relation, disk ages in Lupus have to be comparable to the viscous timescale, on the order of ~ 1 Myr (see also Jones et al. 2012; Rosotti et al. 2017). This viscous timescale is comparable to our models with $\alpha_{\rm visc} = 10^{-3}$ (cf. Table 4.1).

As we made no attempt to match our models to individual observations, it is worthwhile to discuss if it is possible to explain the large disks in our sample, such as IM Lup and Sz 98, by other means than a large $\alpha_{\rm visc}$. A quick comparison with Table 4.1 shows that increasing the disk mass does not help to explain their large $R_{\rm CO,\ 90\%}$. Our models with $M_* = 1.0$ M$_\odot$ and $\alpha_{\rm visc} = 10^{-3} - 10^{-4}$ differ by an order of magnitude in initial disk mass, but at 0.75 Myr they differ by less than 5% in terms of $R_{\rm CO,\ 90\%}$. Another possibility would be increasing the initial disk size $R_{\rm c}(t = 0)$, which we discuss in Section 4.4.2.

Interestingly, five of the seven Upper Sco disks have gas outer radii that lie well below our models with $\alpha_{\rm visc} = 10^{-4}$, indicating that their small $R_{\rm CO,\ 90\%}$ cannot be explained by our models, even when taking into account the uncertainty on their age. As the viscous timescale for our models with $\alpha_{\rm visc} = 10^{-4}$ is already ~ 10 Myr, decreasing $\alpha_{\rm visc}$ does not allow us to reproduce the observed $R_{\rm CO,\ 90\%}$. At face value, these small disk sizes would thus seem to rule out that these disks have evolved viscously. We note, however, that there are processes which, in combination with viscous evolution, could explain these small disk sizes. The first would consist in reducing the CO content of these disks; we discuss this option in Section 4.4.3. Given that the disks in Upper Sco are highly irradiated as members of the Sco-Cen OB association (see e.g. Sections 4.4.4 and Appendix 4.B), another option is that external photo-evaporation is the culprit for their small disk sizes, but we cannot rule out a contribution of MHD disks winds to their evolution.

We have shown that the current observations in Lupus are consistent with viscous disk evolution with a low effective viscosity of $\alpha_{\rm visc} = 10^{-3} - 10^{-4}$ (viscous timescales of $1 - 10$ Myr). However, the current available data do not provide sufficient evidence for viscous spreading, which is the proof that viscosity is driving disk evolution. We stress that this is mostly because most of the available data come from the same star-forming region (Lupus), and therefore most of the disks are concentrated around a disk age range from 1 Myr to 3 Myr. Only a few disks lie outside this range. The inclusion of the Upper Sco disks would help constrain the importance of viscous spreading, but we already commented in the previous paragraph about the caveats with this region. Thus, we conclude that the current sample of radii is insufficient to confirm or reject the hypothesis that disks are viscously spreading. To overcome this problem, future observational campaigns should focus on expanding the observational sample of well-measured disk CO radii in other star-forming regions with a different age than Lupus.

4.4.2 Larger initial disk sizes

In our analysis we assumed that disks start out small, with $R_{\rm init} = 10$ AU, as motivated by recent ALMA observations of disks around young Class 0 and 1 protostars (Maury et al. 2019; Maret et al. 2020; Tobin et al. 2020). However, these observations also show a spread in disk size for these young objects. Increasing the initial disk size would potentially also allow us to explain the larger disks, for example, IM Lup and Sz 98 (see van Terwisga et al. 2018), which have a lower $\alpha_{\rm visc}$.

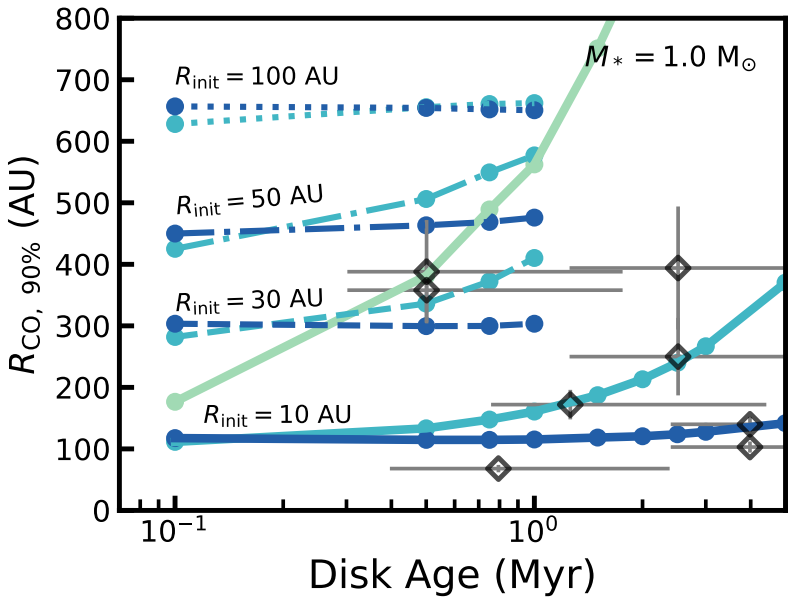

Figure 4.7: Zoom in of the bottom panel of Figure 4.6, showing gas outer radii of our models ($R_{\rm CO,\ 90\%}$) compared to observations. Also added are models with $M_* = 1.0$ M$_\odot$ (see Section 4.2.2) but with $R_{\rm init} = 30, 50$, and 100 AU denoted with dotted, dashed-dotted, and dashed lines, respectively. The colors indicated different values for $\alpha_{\rm visc}$. The new models were only run for $\alpha_{\rm visc} = [10^{-3}, 10^{-4}]$.

Figure 4.7 presents $R_{\rm CO,\ 90\%}$ measured from three sets of models with $M_* = 1.0$ M$_\odot$ (see Section 4.2.2), but with an increased $R_{\rm init} = [30, 50, 100]$ AU. Since our models with $R_{\rm init} = 10$ AU and $\alpha_{\rm visc} = 10^{-2}$ already have $R_{\rm CO,\ 90\%}$ much larger than what is observed, we only run these new models for $\alpha_{\rm visc} = [10^{-3}, 10^{-4}]$. These models have much larger gas disk sizes than models with $R_{\rm init} = 10$ AU; $R_{\rm CO,\ 90\%}$ is at least three times larger ($R_{\rm CO,\ 90\%} \geq 300$ AU). As such, they show that the large disks in the sample ($R_{\rm CO,\ 90\%,obs.} \geq 300$ AU) can also be explained with a larger initial size ($R_{\rm init} = 30$) and a low viscous alpha ($\alpha_{\rm visc} = 10^{-4}$). Extrapolating our results beyond 1 Myr and to models with $M_* = 0.32$ M$_\odot$ there are six examples of such large disks in Lupus that can be explained with $R_{\rm init} \approx 30$ AU (c.f. Figure 4.6). In particular these models show that the observed gas disk sizes of IM Lup and Sz 98 can be explained by either a high viscous alpha ($R_{\rm init} = 10$ AU, $\alpha_{\rm visc} = 10^{-2}$) or a larger initial disk size ($R_{\rm init} \simeq 30 - 50$ AU, $\alpha_{\rm visc} = 10^{-3} - 10^{-4}$). Given the similarities in terms of $R_{\rm CO,\ 90\%}$ between models with $M_* = 1.0$ M$_\odot$ and $M_* = 0.32$ M$_\odot$ seen in Figure 4.3, we expect that increasing $R_{\rm init}$ from 10 AU to 30 AU for models with $M_* = 0.32$ M$_\odot$

would similarly increase their $R_{\mathrm{CO,\ 90\%}}$ by a factor of at least 3.

However, our models show that disks with $R_{\mathrm{init}} = 30$ AU start out at $R_{\mathrm{CO,\ 90\%}} \sim 300$ AU, which is already much larger than most observed $R_{\mathrm{CO,\ 90\%}}$ in Lupus (Ansdell et al. 2018). This indicates that, even if a larger R_{init} can provide an explanation for these six disks, the bulk of the disks in Lupus cannot have had a large R_{init} and they must have started out small ($R_{\mathrm{init}} \simeq 10$ AU). This could be in line with the observations of Tobin et al. (2020), although their measured dust radii should be multiplied by a factor of typically two to three to get the gas radii due to optical depth effects (Trapman et al. 2019).

4.4.3 Effect of chemical CO depletion on measurements of viscous spreading

Over the recent years it has become apparent in observations that protoplanetary disks are underabundant in gaseous CO with respect to the expected abundance of $\mathrm{CO/H_2} = 10^{-4}$ (see, e.g. Favre et al. 2013; Du et al. 2015; Kama et al. 2016b; Bergin et al. 2016; Trapman et al. 2017). Several authors have shown that grain-surface chemistry is able to lower the CO abundance in disks, by converting CO into $\mathrm{CO_2}$ and $\mathrm{CH_3OH}$ on the grains on a timescale of several million years (see, e.g. Bosman et al. 2018; Schwarz et al. 2018). In this work we refer to this process as chemical depletion of CO to distinguish it from simple freeze out of CO, which is included in our models presented in Section 4.3. As the chemical depletion of CO operates on similar timescales as viscous evolution, it can have a large impact on the use of ^{12}CO as a probe for viscous evolution. We implement an approximate description for grain surface chemistry and examine its effects on observed gas outer radii. A more detailed description can be found in Appendix 4.F.

Figure 4.8 shows ^{12}CO 2 - 1 and ^{13}CO 2 - 1 intensity profiles, with and without including chemical CO depletion, for two models at different disk ages. The ^{12}CO 2 - 1 radial intensity profile remains unchanged until 10 Myr, at which point the intensities start to drop between $\sim$ 100 AU and $\sim$ 300 AU, seemingly carving a small "dip" in the intensity profile. With our current definition of the outer radius at 90% of the total flux, this dip lies within $R_{\mathrm{CO,\ 90\%}}$. The decreasing intensity due to chemical CO depletion causes $R_{\mathrm{CO,\ 90\%}}$ to move outward, although the change is small ($\leq 2\%$). The chemical depletion of CO does not affect the CO abundance beyond 300 AU (see, e.g. Figure 4.16), so the ^{12}CO 2 - 1 flux originating from $>$ 300 AU now makes up a larger fraction of the total ^{12}CO flux when comparing models with and without chemical CO depletion. It should therefore be noted that if we were to change our definition of the gas outer radius such that it lies within the "dip", for example, by defining $R_{\mathrm{CO,\ X\%}}$ using a lower percentage of the total flux, $R_{\mathrm{CO,\ X\%}}$ would decrease if we include chemical depletion of CO.

In contrast, the ^{13}CO 2 - 1 intensity profile, shown in the right panels of Figure 4.8, is significantly affected by chemical CO depletion at 10 Myr. Between $\sim$100 AU and $\sim$300 AU the ^{13}CO intensity profile has dropped by more than an order of magnitude. Again, as an consequence of the infinite S/N of our synthetic emission maps, the decrease in the intensity profile has moved the radius enclosing 90% of flux outward. For real observations, in which the S/N is limited, chemical depletion of CO instead significantly decreases the observed outer radius if measured from ^{13}CO emission. Figure 4.8 shows that gas disk sizes measured from ^{13}CO can only be

interpreted correctly if CO depletion is taken into account in the analysis. The figure also highlights the importance of high S/N observations when measuring gas disk sizes from ^{13}CO emission. Given the lack of a significant sample of observed ^{13}CO outer radii, we do not investigate this aspect in this paper further. We note however that once such a sample becomes available, an analysis quantifying the effect of chemical depletion on ^{13}CO outer radii will become possible.

As shown in Figure 4.16, there exists a vertical gradient in CO abundances. Vertical mixing, not included in our models, would move CO rich gas from the ^{12}CO emission layer toward the midplane and exchange it with CO-poor gas. If we were to include vertical mixing, the CO abundance in the ^{12}CO emitting layer would decrease and thus the effect of CO depletion on $R_{\mathrm{CO,\ 90\%}}$ measured from ^{12}CO would increase. The effect would be similar to what is seen for ^{13}CO, indicating that in this case chemical CO depletion could also affect gas disk sizes measured from ^{12}CO emission and should thus be taken into account in the analysis (see, e.g. Krijt et al. 2018; Krijt et al. 2020)

4.4.4 Caveats

Photo-evaporation: In this paper we considered a disk evolving purely under the influence of viscosity. In reality, it is well known that pure viscous evolution cannot account for the observed timescale of a few million years on which disks disperse (see Alexander et al. 2014 for a review). Internal photo-evaporation is commonly invoked as a mass-loss mechanism to solve this problem. Because photo-evaporation preferentially removes mass from the inner disk (a few AUs), it is unlikely to change our conclusions. We note however that some photo-evaporation models (Gorti & Hollenbach 2009) have an additional peak in the mass-loss profile at a scale of 100-200 AU, which might influence our results.

Another potential concern is the effect of external photo-evaporation, that is, mass loss induced by the high-energy radiation emitted by nearby massive stars. In this case, the mass-loss preferentially affects the outer part of the disk (Adams et al. 2004) and might therefore have an influence on the evolution of the outer disk radius, likely moving $R_{\mathrm{CO,\ 90\%}}$ inward. The importance of this effect is region-dependent. A region like Lupus is exposed to relatively low levels of irradiation (see the appendix in Cleeves et al. 2016) and neglecting external photo-evaporation is probably safe in this case, although the effect can still be important for the largest disks (Haworth et al. 2017). For other regions, such as Upper Sco, the impact of external photo-evaporation is potentially more severe since the region is part of the nearest OB association, Sco-Cen (Preibisch & Mamajek 2008). According to the catalog of de Zeeuw et al. (1999), the earliest spectral type in the region is B0 and there are 49 B stars in the complex, suggesting that the level of irradiation can be significantly higher than in Lupus. A simple calculation, outlined in Appendix 4.B, suggests that the disks in Upper Sco are currently subjected to a far-ultraviolet (FUV) radiation field of $10-300$ $\mathrm{G_0}$. For these levels of external UV radiation the mass-loss rate due to external photo-evaporation at radii of ~ 100 AU is $\sim 10^{-9} - 10^{-8}$ $\mathrm{M_\odot yr^{-1}}$, which is of the same order of magnitude as the accretion rate (see, e.g. Facchini et al. 2016; Haworth et al. 2017, 2018). Given the age of the region, stars with even earlier spectral types might have been present but are now evolved, as shown by the red supergiant Antares, implying that in the past the region was subject to a more intense UV flux than it is at the present.

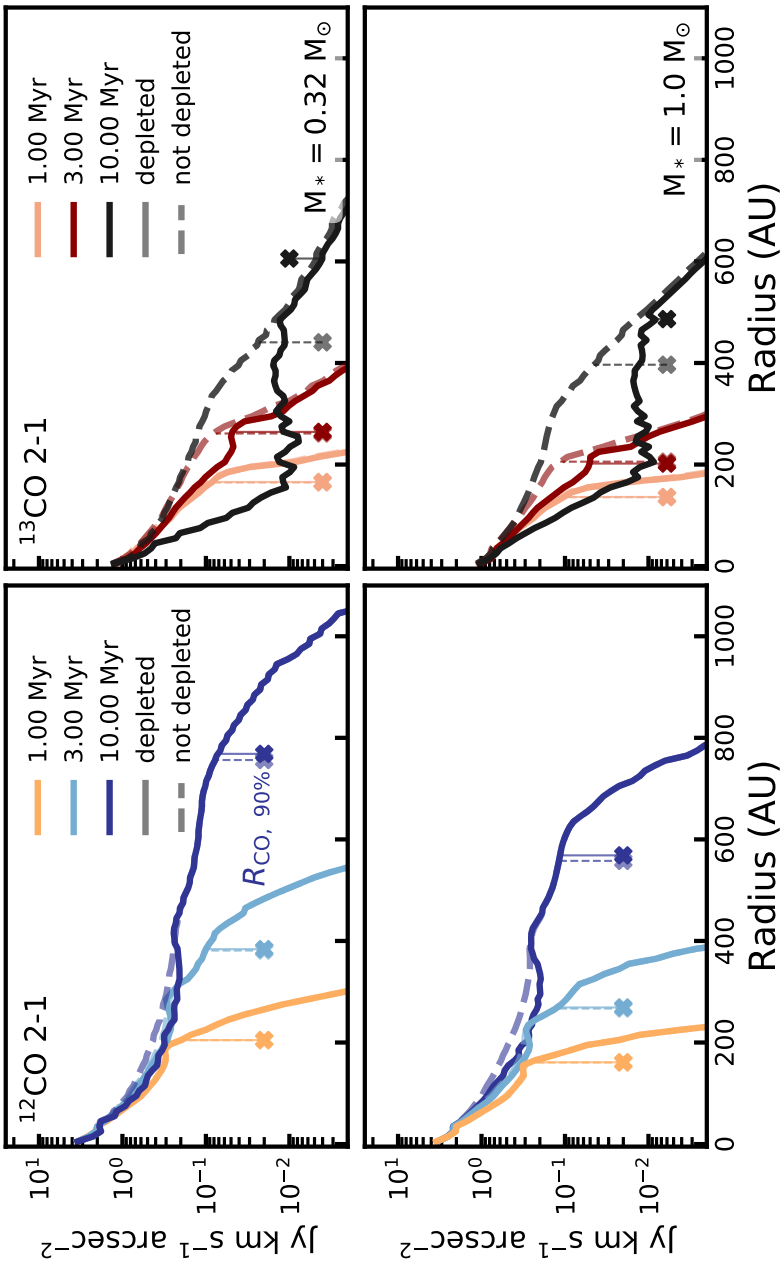

Figure 4.8: Effect of chemical CO depletion through grain-surface chemistry on the ^{12}CO 2-1 intensity profile (left panels) and ^{13}CO 2-1 intensity profile (right panels) after 1 Myr (orange), 3 Myr (light blue/dark red), and 10 Myr (blue/black). The top and bottom rows show models with $M_* = 0.32$ M$_\odot$ and $M_* = 1.0$ M$_\odot$, respectively. The profile without chemical CO depletion is shown as a dashed line. The gas outer radii ($R_{CO,\ 90\%}$) are shown as a cross at arbitrary height below the profile. After 1 Myr the chemical CO depletion is not significant enough to change the intensity profile and $R_{CO,\ 90\%}$. After 10 Myr chemical CO depletion causes $R_{CO,\ 90\%}$ to increase (for details, see Section 4.4.3). Figures 4.13 and 4.17 give a full overview of the ^{13}CO 2-1 intensity profile of the models without and with chemical CO depletion.

Magnetic disk winds versus viscous evolution: In Section 4.4.1 we have shown that the observations in Lupus match with our viscously spreading disk models with $\alpha_{\rm visc} = 10^{-3} - 10^{-4}$. However, we cannot exclude an alternative interpretation in which the observed $R_{\rm CO,\ 90\%}$ and stellar ages of individual disks could be reproduced by models in which disk evolution is driven by disk winds with a suitable choice of parameters. Figure 4.6 should therefore not be considered a confirmation of viscous evolution in disks. To properly distinguish between whether viscous stresses or disk winds are the dominant driver of disk evolution requires an observation of viscous spreading (or lack thereof), that is, that the average disk grows in size over time. Additionally, a search for disk winds in the objects discussed in this paper could allow us to quantitatively compare how much specific angular momentum is extracted by disk winds and how much is transported outward by viscous stresses.

Episodic accretion: In this work we have assumed a simple prescription of viscous evolution, where viscosity in the disk is described by a single parameter $\alpha_{\rm visc}$, which is kept constant in time and does not vary with radius. In reality this is likely to be a too simplistic view. For example, there is an increasing amount of evidence that stellar accretion is episodic rather than the smooth process assumed in this work (see, e.g. Audard et al. 2014 for a review). It is likely however that episodic accretion is most important in the early phases when the star is being assembled, and probably less in the later Class II phase (see, e.g. Costigan et al. 2014; Venuti et al. 2015).

If accretion were also episodic in the Class II phase, the growth of the disk size is likely also to be episodic, rather than the smooth curves shown in this work. However, to reproduce the average observed accretion rate, the episodic accretion rate averaged over time should still match the smooth accretion rate assumed in this work. Observationally, we cannot perform an average over time since the variational timescales, if any exists in the class II phase, are longer than what can be practically measured; observational studies find that accretion is modulated on the rotational period of the star (Costigan et al. 2014; Venuti et al. 2015), but that there is no variation on longer timescales. However, averaging over a sample of similar sources is mathematically equivalent to the average over time since they are at different stages of their duty cycle. Overall, the values for $\alpha_{\rm visc}$ discussed in this work thus should be intended as some kind of average over its variations in space and time.

Related to the topic of episodic accretion is the connection, at an early age, between the disk and its surrounding envelope. Material is accreted from this envelope onto the disk; current evidence indicates that this could still be ongoing into the Class I phase (see, e.g. Yen et al. 2019). While this might affect our results at early ages (0.1-0.5 Myr) it is unlikely to change our results at a later age when accretion from the envelope onto the disk has stopped, and this would be equivalent to changing the initial disk mass or the initial disk size.

4.5 Conclusions

In this work we used the thermochemical code `DALI` to examine how the extent of the CO emission changes with time in a viscously expanding disk model and investigate how well this observed measure of the gas disk size can be used to trace viscous evolution. We summarize our conclusions as follows:

- Qualitatively the gas outer radius $R_{\rm CO,\ 90\%}$ measured from the ^{12}CO emission

of our models matches the signatures of a viscously spreading disk: $R_{\rm CO,\ 90\%}$ increases with time and does so at a faster rate if the disk has a higher viscous $\alpha_{\rm visc}$ (i.e., when it evolves on a shorter viscous timescale).

- For disks with high viscosity ($\alpha_{\rm visc} \geq 10^{-2}$), the combination of a rapidly expanding disk with a low initial disk mass ($M_{\rm disk} \leq 2 \times 10^{-4}$ M$_\odot$) can result in the observed outer radius decreasing with time because CO is photodissociated in the outer disk.

- For most of our models, $R_{\rm CO,\ 90\%}$ is up to $\sim$12 $\times$ larger than the characteristic size $R_{\rm c}$ of the disk, with the difference being larger for more massive disks. As a result, measuring $\alpha_{\rm visc}$ directly from observed $R_{\rm CO,\ 90\%}$ overestimates the true $\alpha_{\rm visc}$ of the disk by up to an order of magnitude.

- Current measurements of gas outer radii in Lupus can be explained using viscously expanding disks with $\alpha_{\rm visc} = 10^{-4} - 10^{3}$ that start out small ($R_{\rm init} = 10$ AU). The exceptions are IM Lup (Sz 82) and HK Lup (Sz 98), which require either a higher $\alpha_{\rm visc} \approx 10^{-2}$ or a larger initial disk size of $R_{\rm init} = 30 - 50$ AU to explain their large gas disk size.

- Chemical depletion of CO through grain-surface chemistry has only minimal impact on the $R_{\rm CO,\ 90\%}$ if measured from ^{12}CO emission, but can significantly reduce $R_{\rm CO,\ 90\%}$ at 5-10 Myr if measured from more optically thin tracers such as ^{13}CO.

We have shown that measured gas outer radii can be used to trace viscous spreading of disks and that models that fully simulate the observations play an essential role in linking the measured gas outer radius to the underlying physical size of the disk. Our analysis shows that current observations in Lupus are consistent with most disks starting out small and evolving viscously with low $\alpha_{\rm visc}$. However, most sources lie within an age range between 1Myr and 3 Myr, which is too narrow to confirm that disk evolution is only driven by viscosity. We therefore cannot rule out that disk winds are contributing to the evolution of the disk. Future observations should focus on expanding the available sample of observe gas disk sizes to other star-forming regions, both younger and older than Lupus, to conclusively show whether disks are viscous spreading and confirm whether viscosity is the dominant physics driving disk evolution.

Appendix

4.A Disk mass evolution

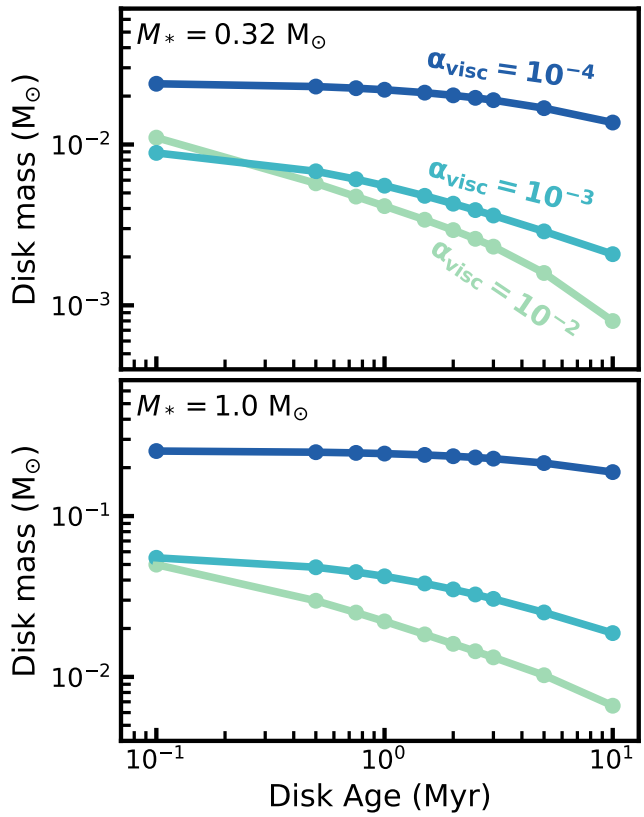

Figure 4.9: Evolution of the disk mass for the models with $M_* = 0.32$ M$_\odot$ and 1.0 M$_\odot$. Evolution of the disk mass for models with $M_* = 0.1$ M$_\odot$ is shown in Figure 4.1. The colors show models with different $\alpha_{\rm visc}$. The order of magnitude difference between the $M_* = 0.32$ M$_\odot$ models (top panel) and $M_* = 1.0$ M$_\odot$ models (bottom panel) are shown.

4.B Local UV radiation field in Upper Sco

Because they belong to the nearest OB association, the disks in Upper Sco are likely to be subjected to high levels of irradiation. In this appendix, we quantify this these irradiation levels using the locations of known B stars (de Zeeuw et al. 1999) and the disks in Upper Sco (see Figure 4.10).

Barenfeld et al. (2016) present ALMA observations of a sample of 106 stars in Upper Sco between spectral types of M5 and G2, selected based on the excess infrared emission observed by *Spitzer* or *WISE* (Carpenter et al. 2006; Luhman & Mamajek 2012). Parallaxes for 96 of these 106 stars were measured with *Gaia* as part of its DR2 data release (Brown et al. 2018). We use these parallaxes to calculate the distance to each of the stars. For the 10 stars in which no parallax is available, we instead assume the distance to be 143 pc, which is the median distance to Upper Sco based on the DR2 data (see, e.g. Bailer-Jones et al. 2018; Wright & Mamajek 2018; Damiani et al. 2019).

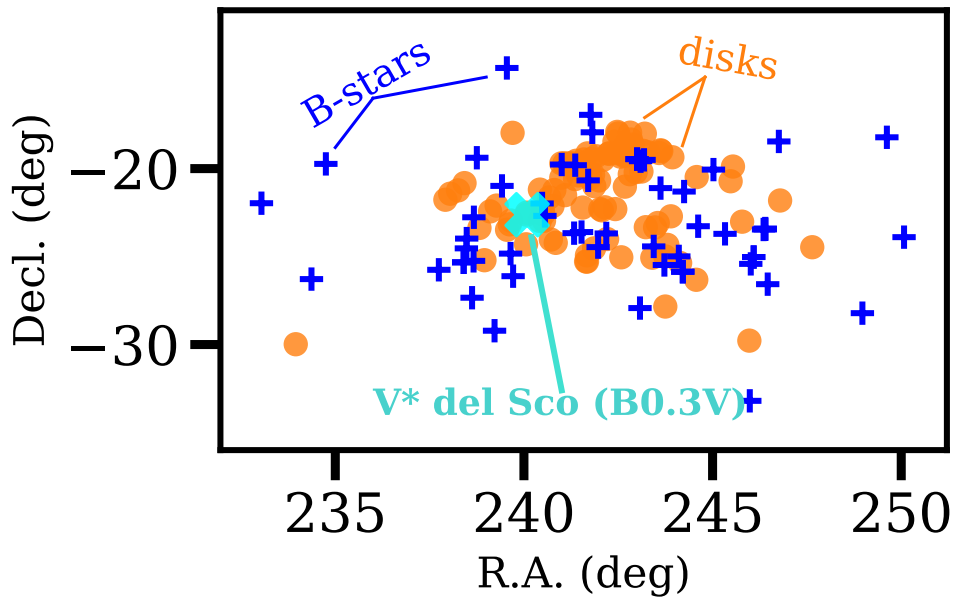

Figure 4.10: Spatial distribution of the disks in Upper Sco (colored circles) and the 49 B stars (blue crosses). The light blue cross denotes the location of V* del Sco, a B0.3V star that contributes significantly to the UV radiation in the region.

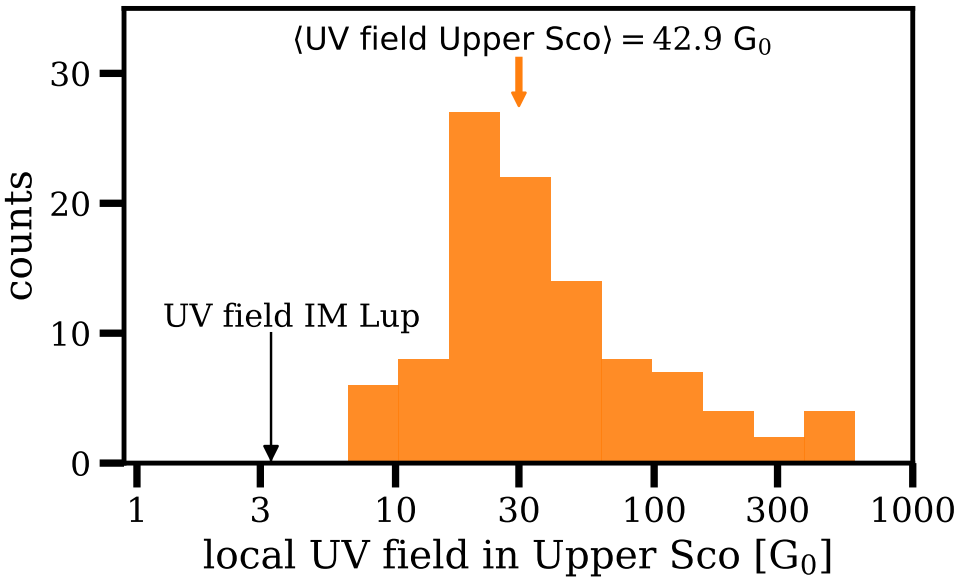

Figure 4.11: Histogram of the local UV radiation field for disks in Upper Sco. Radiation fields were calculated for each disk using Equation (4.10). The orange arrow denotes the median UV radiation field. For comparison, the black arrow shows the external UV radiation field of IM Lup (Cleeves et al. 2016).

In close proximity to these disk-hosting stars there are 49 stars with spectral type B1 and the region hosts one B0.3V star (V* del Sco) (see, e.g. de Zeeuw et al. 1999; de Bruijne 1999). With the exception of the B0 star, these stars are also part of *Gaia* DR2, allowing us to determine distances to these stars based on their parallaxes. The B0 star, V* del Sco, is too bright to be part of *Gaia* DR2. For this star we use a distance of 224 ± 24 pc, which was calculated by Megier et al. (2009) based on interstellar Ca II lines. Combining these positions and distances, we can now calculate, for each disk-hosting star, the relative distances between it and each of the B stars.

To calculate the local FUV radiation field, we take the following approach: We collect the spectral types of the 49 B stars from the catalog of de Bruijne (1999) and use them to compute their effective temperatures following Hillenbrand & White (2004). Based on these effective temperature we fit stellar masses using the stellar models from Schaller et al. (1992). Using the stellar masses we calculate the UV luminosity $L_{\mathrm{UV,\ B\ star}}$ produced by each star based on the relation presented in Buser & Kurucz (1992). Finally, for each disk in the sample from Barenfeld et al. (2016), we calculate the local UV radiation ($F_{\mathrm{UV,\ disk}}$) by adding up the relative contributions of each of the nearby B stars, that is,

$$F_{\mathrm{UV,\ disk}} = \sum_{\mathrm{B\ stars}} \frac{L_{\mathrm{UV,\ B\ star}}}{|x_{\mathrm{disk}} - x_{\mathrm{B\ star}}|^2}, \tag{4.10}$$

where $|x_{\mathrm{disk}} - x_{\mathrm{B\ star}}|$ denotes the relative distance between the disk and the B star.

Figure 4.11 shows a histogram of the local UV radiation $F_{\mathrm{UV,\ disk}}$ for the disks in Upper Sco. Levels range from ~ 8 G_0 to $\sim 7 \times 10^3$ G_0, with a median $F_{\mathrm{UV,\ disk}} = 42.9$ G_0, confirming that these disks are subjected to high levels of external UV radiation. Even the lowest $F_{\mathrm{UV,\ disk}}$ (~ 8 G_0) is several times higher than the external UV field in Lupus (~ 3 G_0; Cleeves et al. 2016).

Owing to the age of Upper Sco (5-11; see Preibisch et al. 2002; Pecaut et al. 2012), stars with spectral types earlier than B0.3, with lifetimes of a few up to 10 Myr might have been present in the region but are now evolved. It is therefore likely that external UV radiation in Upper Sco was higher in the past, suggesting that the $F_{\mathrm{UV,\ disk}}$ calculated in this work is a lower limit of what the disks in Upper Sco experienced during their lifetime.

4.C ^{12}CO radial intensity profiles

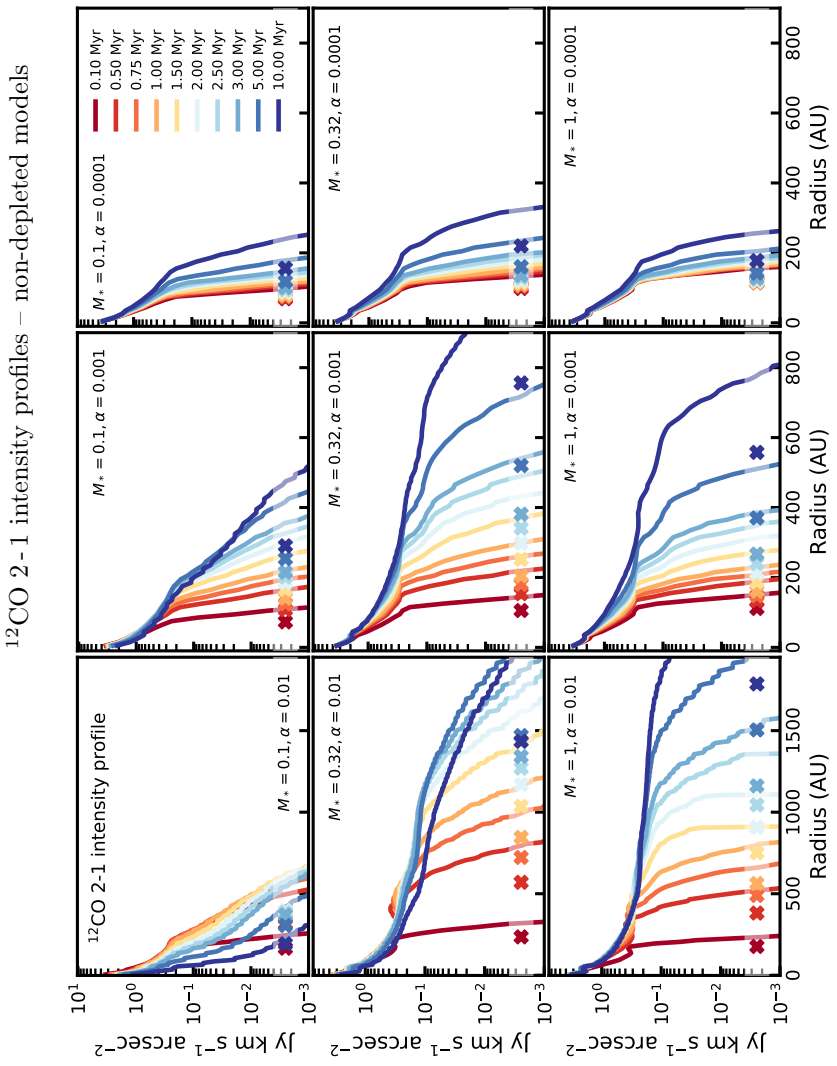

Figure 4.12: Time evolution of the ^{12}CO intensity profiles for our grid of models. The rows show models with equal stellar mass; the columns show models with equal $\alpha_{\rm visc}$. The colors, going from red to blue, show the different time steps. For each model, the radius enclosing 90% of the total flux is denoted by a cross. A low stellar mass corresponds to a low stellar accretion rate, using the observational relation shown in Figure 6 in Alcalá et al. (2017). Also owing to the setup, a low $\alpha_{\rm visc}$ corresponds to a high viscous time ($t_{\rm visc}$) and a high initial mass ($M_{\rm init}$).

4.D Outer radii based ^{13}CO emission

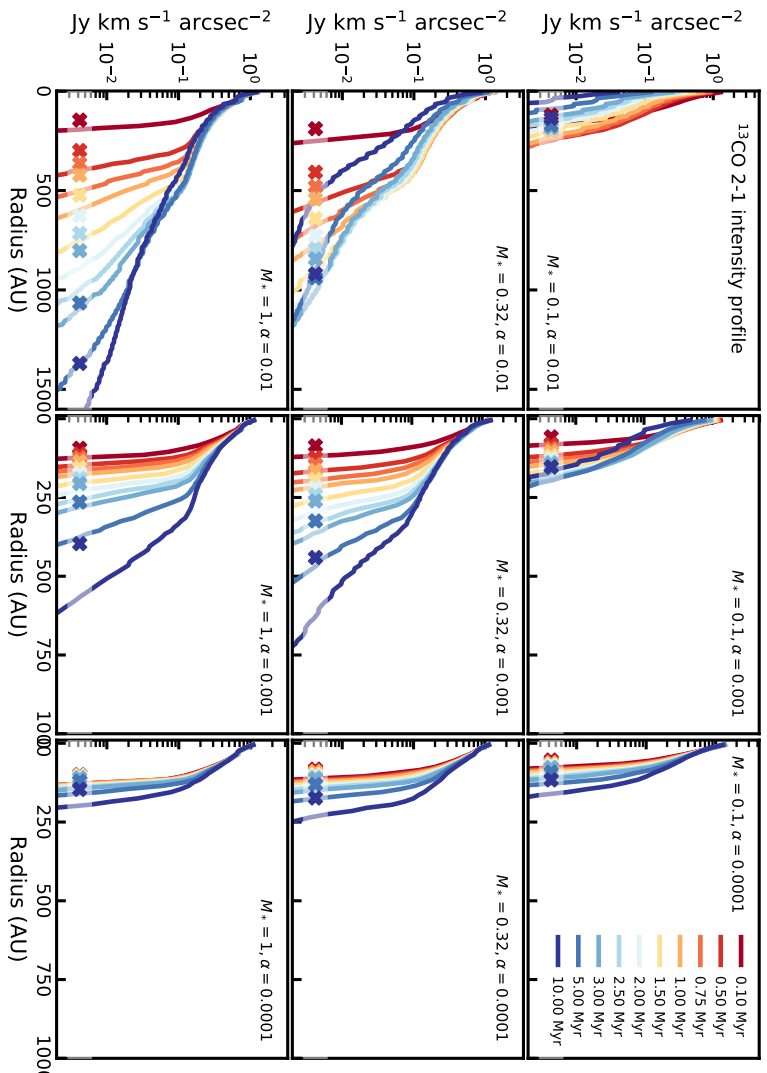

^{13}CO 2 - 1 intensity profiles – non-depleted models

Figure 4.13: Time evolution of the ^{13}CO intensity profiles for our grid of models. The rows show models with equal stellar mass; the columns show models with equal $\alpha_{\rm visc}$. The colors, going from red to blue, show the different time steps. For each model, the radius enclosing 90% of the total flux is denoted by a cross. A low stellar mass corresponds to a low stellar accretion rate, using the observational relation shown in Figure 6 in Alcalá et al. (2017). Also owing the setup, a low $\alpha_{\rm visc}$ corresponds to a high viscous time ($t_{\rm visc}$) and a high initial mass ($M_{\rm init}$).

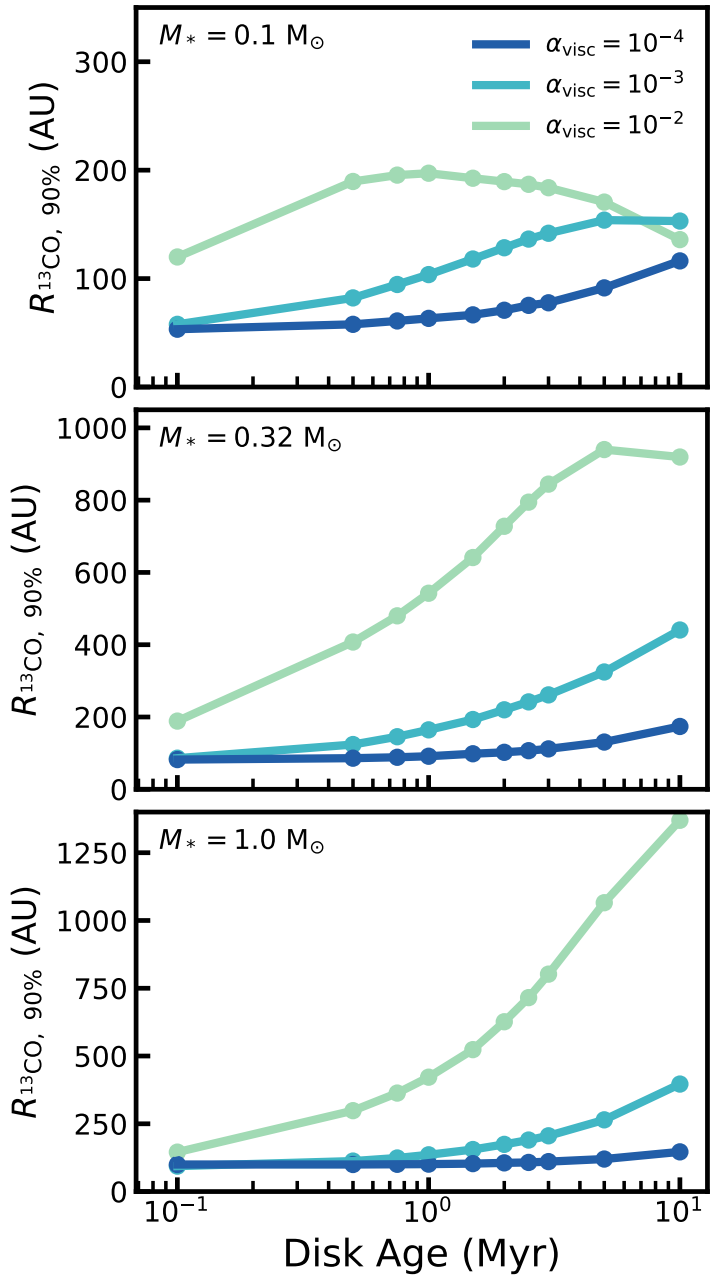

Figure 4.14: Disk ages vs. gas outer radii ($R_{\mathrm{CO,\ 90\%}}$), measured from ^{13}CO 2 - 1 emission. The top, middle, and bottom panels show models with different stellar masses. The colors indicate the α_{visc} of the model.

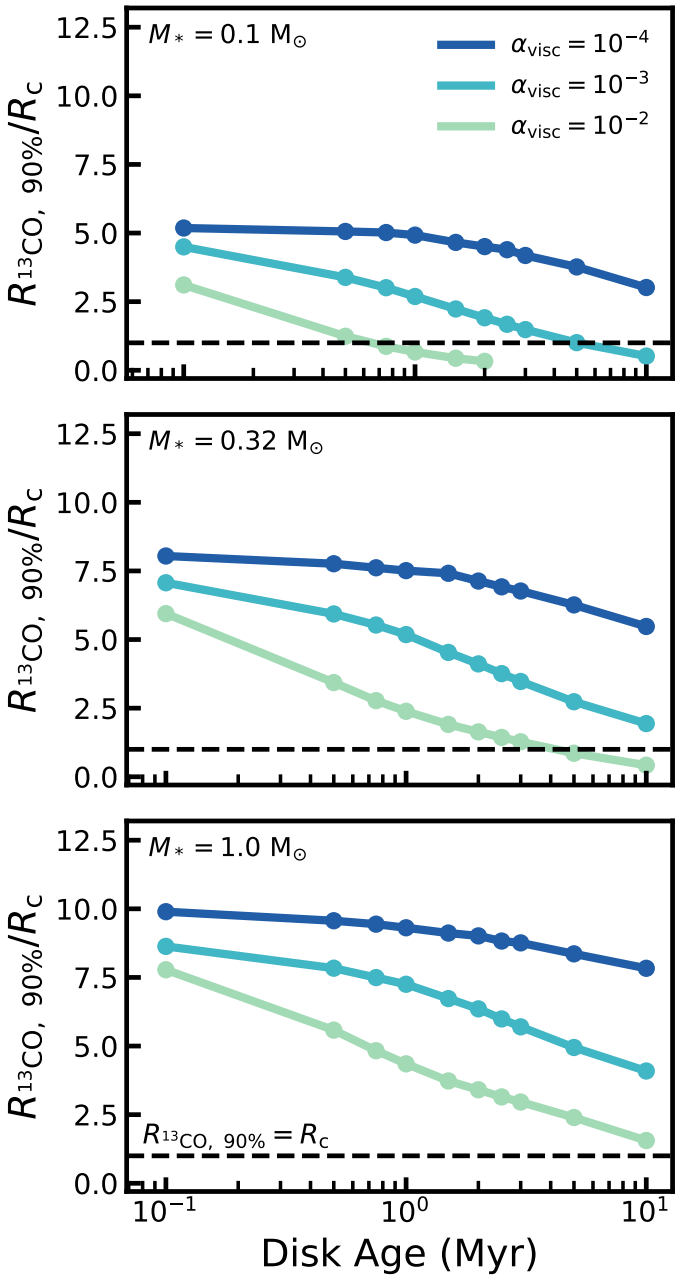

Figure 4.15: Ratio of gas outer radius ($R_{^{13}CO}$) over characteristic radius (R_c) vs. disk age. The gas outer radii are measured from ^{13}CO 2 - 1 emission of our models. The black dashed line indicates where $R_{^{13}CO} = R_c$. The top, middle, and bottom panels show models with different stellar masses. The colors represent models with different α_{visc}.

4.E Observed sample

Table 4.3: Observations in Lupus and Upper Sco

Name	M_* ($M_\odot$)	age (Myr)	$R_{\mathrm{CO,\ 90\%}}$ (AU)
Lupus			
Sz 65	0.70 ± 0.16	$1.3^{+1.9}_{-0.8}$	172 ± 24
Sz 68	2.13 ± 0.34	$0.8^{+0.8}_{-0.4}$	68 ± 6
Sz 71	0.42 ± 0.11	$2.0^{+3.0}_{-1.2}$	218 ± 54
Sz 73	0.82 ± 0.16	$4.0^{+6.0}_{-2.4}$	103 ± 9
Sz 75	0.51 ± 0.14	$0.8^{+1.2}_{-0.5}$	194 ± 21
Sz 76	0.25 ± 0.03	$2.0^{+1.0}_{-1.0}$	164 ± 6
J15560210-3655282	0.46 ± 0.12	$2.0^{+1.0}_{-1.0}$	110 ± 3
IM Lup	1.10 ± 0.0	$0.5^{+0.8}_{-0.3}$	388 ± 84
Sz 84	0.18 ± 0.03	$1.3^{+5.1}_{-0.3}$	146 ± 18
Sz 129	0.80 ± 0.15	$4.0^{+6.0}_{-2.4}$	140 ± 12
RY Lup	1.47 ± 0.22	$2.5^{+2.5}_{-1.3}$	250 ± 63
J16000236-4222145	0.24 ± 0.03	$1.3^{+1.3}_{-0.9}$	266 ± 45
MY Lup	1.02 ± 0.13	$10.0^{+29.8}_{-5.0}$	194 ± 39
EX Lup	0.56 ± 0.14	$2.0^{+1.0}_{-1.0}$	178 ± 12
Sz 133	0.63 ± 0.05	$2.0^{+3.0}_{-1.2}$	238 ± 66
Sz 91	0.47 ± 0.12	$6.3^{+9.5}_{-3.8}$	450 ± 80
Sz 98	0.74 ± 0.20	$0.5^{+0.8}_{-0.3}$	358 ± 52
Sz 100	0.18 ± 0.03	$1.6^{+0.9}_{-1.3}$	178 ± 12
J16083070-3828268	1.81 ± 0.28	$2.5^{+2.5}_{-1.3}$	394 ± 100
V1094 Sco	0.47 ± 0.14	$2.0^{+1.0}_{-1.0}$	438 ± 112
Sz 111	0.46 ± 0.12	$5.0^{+7.6}_{-3.0}$	462 ± 96
Sz 123A	0.46 ± 0.11	$2.0^{+1.0}_{-1.0}$	146 ± 12
Upper Sco			
J15534211-2049282	$0.27^{+0.07}_{-0.05}$	$(5-11)$	$48.3^{+9.6}_{-10.5}$
J16001844-2230114	$0.19^{+0.07}_{-0.04}$	$(5-11)$	$58.2^{+16.1}_{-13.4}$
J16020757-2257467	$0.34^{+0.07}_{-0.06}$	$(5-11)$	$48.9^{+14.1}_{-11.2}$
J16035767-2031055	$1.05^{+0.13}_{-0.11}$	$(5-11)$	$26.3^{+166.3}_{-7.0}$
J16035793-1942108	$0.36^{+0.07}_{-0.07}$	$(5-11)$	$39.4^{+7.7}_{-6.0}$
J16075796-2040087	$0.45^{+0.12}_{-0.09}$	$(5-11)$	$31.3^{+6.4}_{-2.6}$
J16082324-1930009	$0.66^{+0.08}_{-0.06}$	$(5-11)$	$141.1^{+30.8}_{-34.9}$
J16123916-1859284	$0.51^{+0.09}_{-0.08}$	$(5-11)$	$154.2^{+23.5}_{-24.7}$
J16142029-1906481	$0.56^{+0.05}_{-0.06}$	$(5-11)$	$79.4^{+6.3}_{-6.1}$

Table 4.4: Stellar parameters derived from observations presented in Alcalá et al. (2014, 2017) (For the stellar age estimation, see Andrews et al. 2018b). Gas radii for Lupus from Ansdell et al. (2018). Stellar masses for Upper Sco taken from Barenfeld et al. (2016). For the stellar age, the 5-11 Myr stellar age of Upper Sco is used (see, e.g. Preibisch et al. 2002; Pecaut et al. 2012). For sources in Upper Sco $R_{\mathrm{CO,\ 90\%}}$ were calculated from the fit to the observed ^{12}CO intensity in Barenfeld et al. (2017).

4.F Implementing CO chemical depletion through grain-surface chemistry

Based on the results from Bosman et al. (2018), we developed an approximated description for CO grain surface chemistry. The description only traces the main carbon carriers, that is, CO, CH_3OH, CO_2, and CH_4. Briefly, the approximation splits reactions into two groups, fast and slow reactions, and assumes that fast reactions can be calculated by equilibrium chemistry and that only the slow reactions need to be integrated explicitly. A more detailed description is provided in appendix A of Krijt et al. (2020). The approximation breaks down in the upper regions of the disk, where photodissociation of CO by UV photons becomes important. In these regions the chemistry included in `DALI` provides more accurate CO abundances. We therefore split our disk models into two regions based on the outward CO column:

$N_{\rm CO} < 10^{16}$ cm^{-2}**;** the outward CO column is too low for CO to self-shield against photodissociation. As a result the CO chemistry is accurately described by the photochemistry included in DALI and we therefore do not recompute the CO abundances.

$N_{\rm CO} \geq 10^{16}$ cm^{-2}**:** Deeper in the disk CO is able to self-shield against photodissociation. Grain-surface chemistry is able to convert CO into other species, thus lowering the gas-phase abundance of CO. For this region we recompute the CO abundances using the approximate grain-surface chemistry from Krijt et al. (2020)

Figure 4.16 presents the CO abundance structure with and without including CO depletion through grain-surface chemistry. At 1 Myr, shown in left panels, the inclusion of grain-surface chemistry has little impact on the CO abundance. However, at 10 Myr CO has become significantly depleted (X[CO] $\leq 10^{-8}$) around the midplane of the disk. We obtain the same conclusion as Bosman et al. (2018), namely that CO depletion only becomes significantly long timescales. Among our models we are only starting to see its effects after $\geq$ 5 Myr, indicating this process is most important for older star-forming regions such as Upper Sco.

Figure 4.16 also shows the emitting layers of ^{12}CO 2 - 1 and ^{13}CO 2 - 1. The chemical conversion of CO into other species predominantly takes place around the midplane, while the CO emitting layer is higher up in the disk. For ^{12}CO 2 - 1 the emitting layer lies predominantly in the region of the disk, where the CO abundances are set by photodissociation and not grain-surface chemistry, and are therefore only slightly affected by CO chemistry after 10 Myr. The emitting layer of ^{13}CO 2 - 1 lies deeper in the disk and is therefore significantly affected by the conversion of CO.

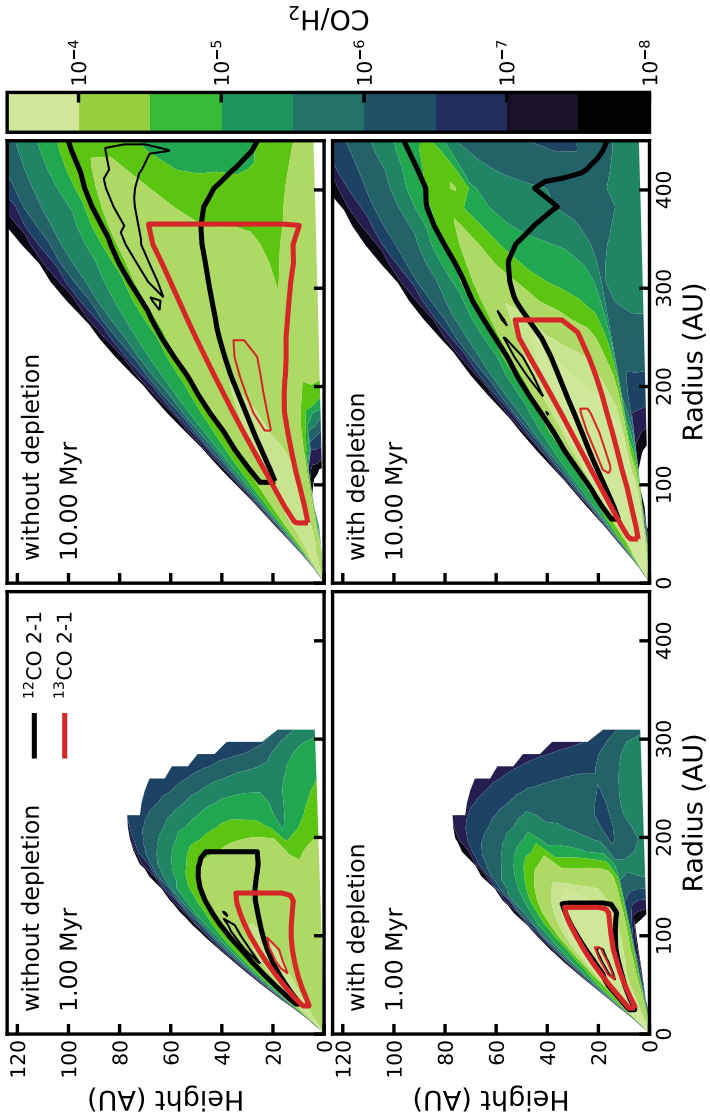

Figure 4.16: Effect of chemical depletion of CO through grain-surface chemistry on the CO abundance after 1 Myr (left panels) and 10 Myr (right panels). The example model shown has $M_* = 0.32$ $M_\odot$ and $\alpha_{\rm visc} = 10^{-3}$. The colors show the CO abundance with respect to H_2, where white indicates $CO/H_2 \leq 10^{-8}$. The black contours show the ^{12}CO 2-1 emitting region, enclosing 25% and 75% of the total ^{12}CO flux. Similarly, the red contours show the ^{13}CO 2-1 emitting region.

4.G Effect of CO depletion on the ^{13}CO emission

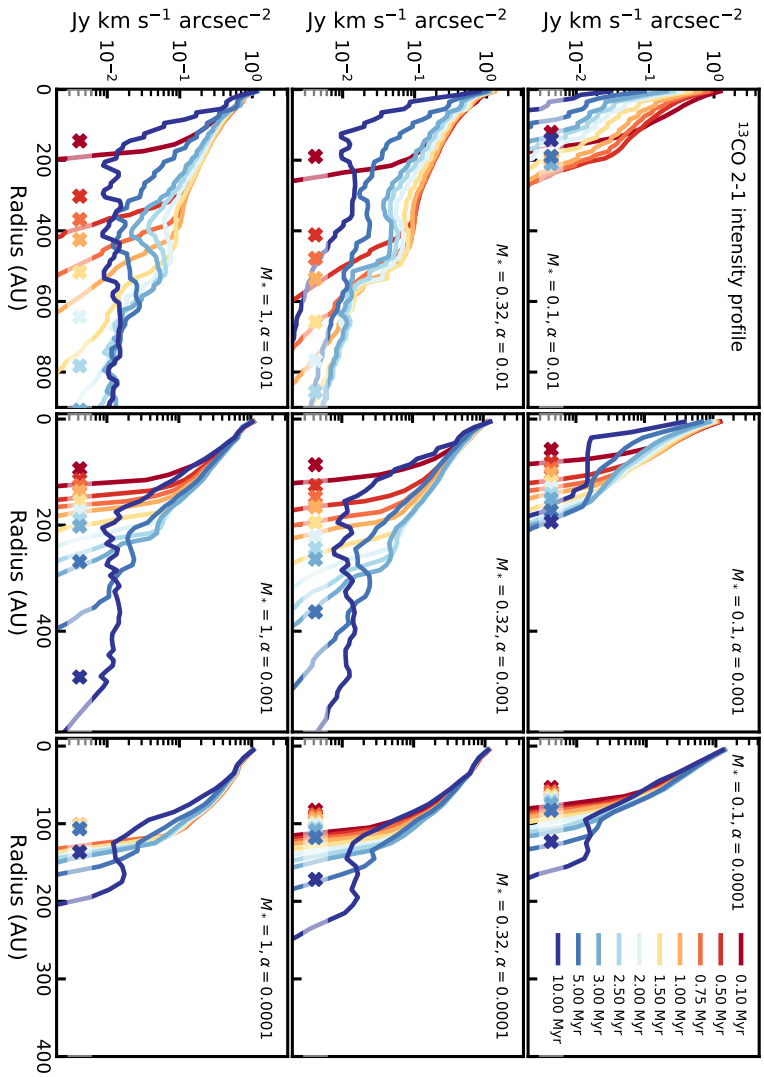

Figure 4.17: Time evolution of the ^{13}CO intensity profiles for our grid of models, after including the effects of chemical depletion of CO through grain surface chemistry (see Sections 4.4.3 and 4.F). The rows show models with equal stellar mass, columns show models with equal $\alpha_{\rm visc}$. The colors, going from red to blue, show the different time steps. For each model, the radius enclosing 90% of the total flux is indicated by a cross. A low stellar mass corresponds to a low stellar accretion rate, using the observational relation shown in Figure 6 in Alcalá et al. (2017). Also owing to the setup, a low $\alpha_{\rm visc}$ corresponds to a high viscous time ($t_{\rm visc}$) and a high initial mass ($M_{\rm init}$).